Unravelling the morphogenesis of coastal terraces at Cape Laundi (Sumba Island, Indonesia): insights from numerical models

Keywords:

Numerical modeling, Geomorphology, Sea level, Marine Isotopic Stage, Coastal terrace.

Abstract

The morphology of coastal sequences provides fundamental observations to unravel past sea level (SL) variations. For that purpose, converting morphometric observations into a SL datum requires understanding their morphogenesis. The long-lasting sequence of coral reef terraces (CRTs) at Cape Laundi (Sumba Island, Indonesia) could serve as a benchmark. Yet, it epitomizes a pitfall that challenges the ultimate goal: the overall chronology of its development remains poorly constrained. The polycyclic nature of the terraces, involving marine erosion and reoccupation of old coral colonies by more recent ones hinders any clear assignment of Marine Isotope Stages (MIS) to specific terraces, in particular the reference datum corresponding to the last Interglacial maximum (i.e., MIS 5e). Thus, to overcome these obstacles, we numerically model the genesis of the sequence, testing a range of eustatic SL reconstructions and uplift rates, as well as exploring the parameter space to address reef growth, erosion, and sedimentation. A total of 625 model runs allowed us to improve the morpho-chronological constraints of the coastal sequence and, more particularly, to explain the morphogenesis of the several CRTs associated with MIS 5e. Our results suggest that the lowermost main terrace was first constructed during the marine transgression of MIS 5e and was later reshaped during the marine regression of MIS 5e, as well as during the MIS 5c and MIS 5a highstands. Finally, we discuss the general morphology of the sequence and the implications it may have on SL reconstructions. At Cape Laundi, as elsewhere, we emphasize the necessity of addressing the development of CRT sequences with a dynamic approach, i.e., considering that a CRT is a landform built continuously throughout the history of SL oscillations, and not simply during a singular SL maximum.

1. Introduction

Since the 19th century, sequences of coral reef terraces (CRTs) have been described in the Caribbean province (e.g., Crosby, 1883; Peñalver et al., 2021), in the Indo-Pacific province (e.g., Darwin, 1842; Pedoja et al, 2018), as well as alongshore the Red Sea (e.g., Hume and Little, 1928; Obert et al., 2019). Altogether, they provide a valuable database to infer sea level (SL) oscillations during the Quaternary, both on a local/regional level (relative sea level; RSL) and on a global level (eustatic sea level; ESL)

(Pedoja et al., 2011, 2014; Rovere et al., 2016a). Owing to their exceptional preservation and longevity, a few of those are benchmarks to ESL studies (e.g., Barbados, Thompson and Goldstein, 2005; Huon Peninsula, de Gelder et al., 2022). Surprisingly, the long-lasting emerged coastal sequence of Cape Laundi (Sumba Island, Indonesia), including at least 18 successive CRTs and encompassing the last million years (e.g., Pirazzoli et al., 1991), is not included in these. The main reasons for this are the diachronic nature and the particularly rounded cross-shore morphology of the Cape Laundi CRTs, challenging any reciprocal association of a terrace with a discrete SL highstand. Indeed, various dating methods (U/Th; Electron Spin Resonance, ESR) yield discrepant ages of the coral colonies within a unique CRT (e.g., Bard et al., 1996). Conversely, previous dating also revealed similar ages on several distinct CRTs. For example, ages of dated coral colonies ascribed to Marine Isotopic Stage (MIS) 5e have been found on at least three different CRTs (Pirazzoli et al., 1991; Bard et al., 1996). Such observations challenge the common bijective approach, i.e., one-to-one pairing of a terrace and a SL highstand.

Here, in order to rehabilitate the Cape Laundi sequence for SL studies, we explore the genetic links between ESL oscillations and the morphogenesis of this sequence using a kinematic model based on reef morphology (Husson et al., 2018; Pastier et al., 2019). We perform a parametric study using five ESL curves (Waelbroeck et al., 2002; Bintanja et al., 2005; Rohling et al., 2009; Grant et al., 2014; Spratt and Lisiecki, 2016) and a range of model parameters, including uplift rate, basement slope, reef growth rate and marine erosion rate. From a set of 625 simulations, based on 8 morphological and chronological criteria, we selected the best-fit to the Cape Laundi sequence for each ESL curve. This further permits us to bracket the range of admissible parameters and to assign ages for each CRT. We more specifically focus on the presence of several CRTs associated with MIS 5e. We explain the overall morphology of the sequence and in particular the roundness of distal edges of CRTs at Cape Laundi. Finally, our study unravels the complex nature of CRTs, emphasizing the need to apply a dynamic approach to understand their morphogenesis.

2. Geomorphological setting and previous observations

Sumba Island is located in the lesser Sunda-Banda arc (Fig. 1A), at the transition from oceanic subduction in the West, along the Java trench, to the collision of the Banda arc with the continental Indian-Australian plate in the East (Hinschberger et al., 2005). Since the Late Miocene, the convergence between Eurasia and the Indian-Australian plate shortened and uplifted the fore-arc domain, where Sumba Island stands (e.g., Fortuin et al., 1997; Haig, 2012; Tate et al., 2014; Husson et al., 2022). The Cretaceous to Oligocene crystalline basement is almost entirely covered by Miocene and Pliocene deposits (Abdullah et al., 2000), bordered by a ~350 km long emerged sequence of CRTs that record the interplay between local SL variations and Quaternary uplift (e.g., Pirazzoli et al., 1991; Bard et al., 1996; Nexer et al., 2015). The sequence spans approximately two-thirds of the island shores. It is continuous all along the northern shore of the island, only locally interrupted by large rivers (Fleury et al., 2009; Nexer et al., 2015; Authemayou et al., 2018; Chauveau et al., 2021a). To the south of the island, only a small CRTs sequence has been described (Authemayou et al., 2022).

On the northeast coast of Sumba, live coral colonies are exclusively found on the reef crest and on the fore reef slope (diving observation). The reef is comprised of a few *Porites sp.* and branching corals (Hantoro, 1992). The back reef and reef flat are characterized by a low density of live corals (i.e., coral cover < 10 %), mainly shallow species that are resistant to episodic emergence and/or relatively high-water turbidity (e.g., *Goniastrea retiformis*, *Acropora digitifera*; Bard et al., 1996) and by a coralgal environment.

The Cape Laundi sequence in the central part of the northern shore reaches ~470 m in elevation and has a staircase morphology with six main CRTs separated by continuous high cliffs (> 10 m; Fig. 1B, Jouannic et al., 1988; Pirazzoli et al., 1991). Most main CRT includes several intermediate CRTs, that have a more diffuse morphology with surfaces and discontinuous cliffs weakly sloping shoreward, and rounded distal parts (Hantoro et al., 1989; Pirazzoli et al., 1993). The CRTs below CRT III are narrower and more seaward sloping than those above (Fig. 1; e.g., Chauveau et al., 2021a, 2021b). The main and intermediate CRTs are indicated by Roman numbers (e.g., CRT I) and with lower-case numbers (CRT I_1), respectively.

Coral colonies from the surface of the four lowest main CRTs have been dated (U/Th and ESR; Jouannic et al., 1988; Pirazzoli et al. 1991; Bard et al., 1996). All ages were correlated to the ESL peaks of their associated ESL highstands: MIS 15 (610 ± 10 ka), MIS 11 (390 ± 30 ka), MIS 9 (325 ± 18.5 ka), MIS 7 (239.5 ± 8.5 ka), MIS 5e (122 ± 6 ka), MIS 5c (100 ± 5 ka), MIS 5a (82 ± 3 ka), and MIS 1 (Pirazzoli et al., 1993; Bard et al., 1996). The oldest dated CRT (V) has ESR ages of 584 ± 88 ka and 603 ± 90 ka and was ascribed to MIS 15. The ages of the successive upper CRTs were extrapolated assuming constant uplift rate (0.49 ± 0.01 mm a^{-1}), and thereafter associated with ESL maximums up to ~1 Ma (MIS 29; Pirazzoli et al., 1993).

Several temporal discrepancies arose within the earliest dataset from a bijective perspective (Pirazzoli et al., 1993). First, multiple U-series ages of corals were found on the same CRT, and thus related to substages of the same MIS. For example, ages of ~82 ka (MIS 5a) and ~138 ka (MIS 5e) are obtained from coral colonies sampled on CRT I_1. Second, U-series ages related to MIS 5e were found on corals from at least three distinct CRTs (138 ± 9 on CRT I_1; 114 ± 7, 119 ± 18, 120 ± 8, 124 ± 19, 136 ± 8, 142 ± 21 on CRT I_2; 148 ± 14, 117 ± 18, 133 ± 7 on CRT II_1; Pirazzoli et al., 1993). Finally, U-series ages and ESR ages of corals from the same CRT do not always match with one another (e.g., 148 ± 14 and 275 ± 41 on CRT II_1). Thermal Ionisation Mass Spectrometry (TIMS) dating of corals (Bard et al., 1996) specified the diachronicity (i.e., ages associated to MIS 5a, 5c, and 5e on CRT I_1; MIS 5c and 5e ages on CRT I_2). Previous authors (Jouannic et al., 1988; Pirazzoli et al., 1993; Bard et al., 1996; Chauveau et al., 2021b) pointed at the diachronism on the lowermost CRT I and inferred its composite nature, implying both constructive and erosive reoccupation. Pirazzoli et al. (1993) suggested that local SL fluctuations superimposed over a regular uplift rate of 0.5 mm a^{-1} must have caused recurrent reoccupations of RSL over antecedent reefal constructions, capable of reworking sediments, fostering abrasion or further developing bioconstructions differing in age by as much as 100 ka on the same CRTs.

3. Materials and Methods

In this section, we explain, **1)** what CRTs sequences are, **2)** how we collected and processed our field data, **3)** the numerical model used, and **4)** how we selected the most robust previous dating.

3.1. CRTs sequences

CRTs are largely encountered in the tropical zones (Schwartz, 2006; Cabioch, 2011; Pedoja et al., 2011; 2014; Murray-Wallace and Woodroffe, 2014). When ESL falls too rapidly and/or when the reef is uplifted by tectonic movements or glacial isostatic adjustment (GIA), the reef (mainly fringing reefs) emerges and fossilizes, forming a CRT. The joint effects of ESL oscillations, vertical land movement and reef accretion and erosion can result in the generation of staircase CRT sequences (Fig. 2; e.g., Chappell, 1974; Pirazzoli, 2005).

CRTs are expanses of reefal limestone with flat or slightly sloping surfaces, limited seaward by a distal edge over a cliff with variable height (Fig. 2; e.g., Pirazzoli et al., 1991). The cliff separating successive CRTs is either an erosional sea-cliff, a former fore-reef slope (sometimes very gentle as in Cape Laundi), or a combination of both (e.g., Chappell, 1974). Landward, the inner edges of CRTs are characterized by a break in slope, sometimes interpreted as a shoreline angle, and occasionally associated with an erosional notch (e.g., Speed and Cheng, 2004; see Fig. 3 in Pedoja et al., 2018). In general, the elevation of a CRT taken as a reference point for RSL calculations corresponds to its average elevation, its inner edge, or, if present, to the elevation of the highest *in situ* corals that are usually found on the paleo reef crest (Rovere et al., 2016b). However, for most of the Cape Laundi CRTs, the difference in elevation between the inner and distal edges is too important (i.e., from a few meters to ~40 m for CRT IV) to consider that the average elevation of the CRT is representative of the paleo reef or that the distal edge corresponds to the paleo reef crest. Recently, Chauveau et al. (2021b) analyzed the concentration of the cosmogenic nuclide ^{36}Cl of 34 samples of surface limestone taken throughout the CRT sequence and on different morphological parts (i.e., the main surfaces, inner and distal edges of CRTs). The results highlighted that the distal edge of CRTs is affected by higher continental denudation rates than the other proximal parts (i.e., the main surface and the inner edge of CRTs). In addition, we consider here that the width and height of a CRT correspond respectively to the horizontal distance and elevation difference between the two adjacent inner edges (Fig. 2).

The morphology and stratigraphy of CRTs result from interactions between reef accretion (bioconstruction and sedimentation), marine erosion, RSL change (local SL variations and vertical land motion), subaerial processes and geometry of the basement (e.g., Pirazzoli, 2005; Cabioch, 2011; Husson et al., 2018; Pedoja et al., 2018; Pastier et al., 2019; Chauveau et al., 2021b). These numerous interactions account for a wide spectrum of CRT morphologies (Fig. 2). At Cape Laundi, one CRT with a continuous high fossil sea cliff (> 10 m; see CRT I in Fig. 2) can include numerous secondary or intermediate CRTs (CRTs I_1 and I_2 in Fig. 2) with or without low (< 10 m), eroded, fossil sea cliffs and multiple associated reefal limestone units (RLUs; Hantoro et al., 1989; Pirazzoli et al., 1993). We refer to these landforms as main CRTs (Fig. 2; e.g., Chauveau et al., 2021b).

Theoretically, when these main CRTs include several intermediate CRTs but are formed by only one RLU (main CRT II on the Profile 1 in Fig. 2), we call them compound main CRTs (see Fig. 2 in Pedoja et al., 2014). On the contrary, when a CRT does not include intermediate CRTs but is formed by several RLUs (see main CRTs I and II on the Profile 2 in Fig. 2), associated to distinct RSL highstands, we call it composite CRT (see Fig. 3 in Pedoja et al., 2018). Finally, when a main CRT includes several intermediate CRTs and is formed by several RLUs (main CRT I on the Profile 1 in Fig. 2), we call it compound and composite main CRT.

3.2. Onshore and offshore morphometry

We manually mapped the inner and distal edges of CRTs at Cape Laundi, following the breaks in the slope (as described in section 3.1.), using a 2 m resolution Digital Elevation Model (DEM) and the resulting slope (Fig. 1B) and hillshade maps. This DEM has been produced from stereoscopic satellite images (Pleaides, CNES) with MicMac freeware (e.g., Rupnik et al., 2016). To assess the lateral continuity of the CRTs sequence, we used stacked swath profiles (Armijo et al., 2015; Fernández-Blanco et al., 2019), constructed using 600 parallel swath profiles (Fig. 3) to derive a 2.5-D view of the landscape. On swath profiles, CRTs are revealed by areas with clusters of overprinted topographic profiles that are indicative of the flatness of the topography.

We acquired topographic and bathymetric profiles, using a real kinematic differential global positioning system (RTK dGPS) onshore (elevations are converted to orthometric heights, following Boulton and Stokes, 2018), and a Humminbird 700 series sonar offshore (Figs. 1B; 3B). Onshore, our profiles are parallel to the profile investigated by Pirazzoli et al. (1993) and runs perpendicular to the inner edges of the successive CRTs. Profile 1 crosses the whole sequence while Profile 2 is designed to focus on the lowest CRTs (Figs. 1B; 3B). Here, taking advantage of the high-resolution topographic data (Pleiades imagery, DEM and dGPS), we revised the nomenclature of CRTs (Table 1). We assigned an elevation uncertainty to all field measurements as a function of the observed roughness of the landform (± 0.5 m below 250 m; ± 1.5 m above 250 m, as defined in Chauveau et al., 2021b). In this study, all elevations are given relative to mean sea level (msl).

Nomenclature of the CRTs		**MIS associated with CRTs**		**Elevation of CRTs**	
Pirazzoli et al. (1991, 1993)	**This study**	**Pirazzoli et al. (1991, 1993)**	**This study**	**Pirazzoli et al. (1991, 1993) (Elevation of former reef crest; m)**	**This study (Elevation of inner edge; dGPS ; m)**
CRT O1	CRT 0	MIS 1	MIS 1	1.1 ± 0.5	0 ± 0.5
CRT I1	CRT I1	MIS 5	MIS 1; 5a; 5c	3.5 ± 0.5	6.4 ± 0.5
CRT I2	CRT I2	MIS 5	MIS 5c; 5e	19 ± 1	23.2 ± 0.5
CRT II1	CRT II0	MIS ?	MIS 5e		42.4 ± 0.5
CRT II2	CRT II1	MIS 5; 7	MIS 5e	50 ± 5	57.1 ± 0.5
CRT II3	CRT II2	MIS 5; 7; 9	MIS 5e; 7a; 7c	62 ± 5	76.0 ± 0.5
CRT II4	CRT II3	MIS 7; 9	MIS 7c; 7e		79.9 ± 0.5
	CRT II4				95.0 ± 0.5
CRT II5	CRT II5	MIS 9	MIS 9a; 9c/e		105.4 ± 0.5
	CRT II6				119.3 ± 0.5

CRT III1	CRT II7	MIS 9	MIS 9c/e	145 ± 10	136.6 ± 0.5
CRT III2	CRT III	MIS 11	MIS 11		165.4 ± 0.5
CRT III3	CRT IV	MIS 13	MIS 13		250.5 ± 1.5
CRT IV1; IV2	CRT V	MIS 15; 17	MIS 15; 17	275 ± 10	341.0 ± 1.5
CRT IV3; V0; V1; V2	CRT VI	MIS 19; 21; 23	MIS 19; 21; 23		389.3 ± 1.5
CRT VI1; VI2	CRT VII	MIS 25; 27; 29	MIS 25; 27; 29		470 ± 1.5

Table 1. Nomenclature (from Pirazzoli et al., 1991, 1993, and revised in this study), associated MIS (i.e., Marine Isotopic Stage), elevation, width of CRTs from previous studies (Pirazzoli et al., 1991, 1993), dGPS (i.e., differential Global Positioning System) field measurements. The uncertainties of the elevation of former reef crests are those given by Pirazzoli et al (1991, 1993). Those of the inner edges correspond to the roughness of the terraces (as in Chauveau et al., 2021b).

3.3. Modeling CRTs sequences

Since the earliest work of Chappell (1980), many other numerical models of reef growth have been developed (e.g., Bosscher and Schlager, 1992; Turcotte and Bernthal, 1984; Webster et al., 2007; Koelling et al., 2009; Toomey et al., 2013). Here, we use a kinematic profile evolution model, combining the effects of reef growth, marine erosion, and deposition of subsequent clastic sediments (Husson et al., 2018; Pastier et al., 2019). $\frac{ds}{dt}$, the variation of the elevation profile (ds) through time (dt), is defined by:

$$\frac{ds}{dt} = \frac{dG}{dt} + \frac{dE}{dt} + \frac{dS}{dt} + U \quad (1)$$

Where $\frac{dG}{dt}$, $\frac{dE}{dt}$ and $\frac{dS}{dt}$ respectively represent the contribution of reef growth, marine erosion, and clastics deposition. U is the vertical land motion rate. The effective reef growth rate, G, is defined by a maximum potential reef growth rate G_{max}, modulated by a vertical factor γ and a horizontal factor ζ:

$$\frac{dG}{dt} = G_{max} \times \gamma \times \zeta \quad (2)$$

The vertical factor γ accounts for decreasing coral growth rate with increasing water level due to light attenuation. It is controlled by the local water depth along the profile, h(s), and a maximum water depth for significant coral growth, h_{max}:

$$\gamma = \frac{1}{2}(1 + \cos\frac{\pi\, h(s)}{hmax}) \tag{3}$$

The horizontal factor, ζ, accounts for decreasing coral growth from the reef crest shoreward. It is controlled by the horizontal distance to the open water (x_{ow}-x, where x_{ow} is defined by the first occurrence of the optimum water depth for reef growth and x the horizontal position along the profile) and δ setting the horizontal tension for reef growth decay from the open ocean (see Fig. 1 and Table 1 in Pastier et al., 2019):

$$\zeta = \frac{1}{2}(\,1 + \tanh\frac{xow - x}{\delta}) \tag{4}$$

In practice, the effective reef growth rate (i.e., G) is systematically lower than the maximum potential growth rate (i.e., G_{max}) because of the penalties γ and ζ applied to G.

Marine erosion is based on the wave erosion model of Anderson et al. (1999), consisting of a vertical sea-bed erosion component and a horizontal cliff erosion component. E is defined as the erosional potential, accounting the tidal and wave energy but also on chemical and biological agents (Pastier et al., 2019). This value is express as an effective eroded volume per unit of time and per unit of coastline length. E dissipates from the open ocean towards the shore, so that the erosional residual power E_r gradually decreases towards the shore. Thus, a fraction of E_r erodes the foundation at each location along the profile. This fraction of E_r depends on the local water level, h, the water depth for wave base erosion, h_{wb}, and a coefficient for sea bed erodibility K (= 0.1 (bedrock) or 1 (notch); Pastier et al., 2019), such as:

$$\frac{dEr}{dt} = K \times Er \times \exp\left(-\frac{h}{hwb}\right) \quad (5)$$

Then, a residual power (defined as $E - \frac{dEr}{dt}$ in Pastier et al., 2019) serves to carve a 1 m high notch and all the overhanging material collapses to form a cliff.

In the model, the clastic sedimentation redistributes the eroded material (bedrock, notch and fallen cliff) from the shore towards the ocean and starting at h_{wb}. Clastic deposition occurs horizontally in lagoons, if any, up to h_{wb}. The remainder is transported further seaward along an arbitrary repose angle of 10 % at the foot of the forereef slope. The initial profile is imposed as a linear slope (α). The temporal and spatial resolution are respectively 1 ka and 1 m (see Pastier et al. (2019) for more details).

Local SL variations are equally crucial. Yet, uncertainties in Quaternary ESL variations are high (Fig. 4; e.g., Caputo, 2007) and the choice of a specific ESL or RSL curve may greatly affect the model outcome (e.g., De Gelder et al., 2020). We chose five reconstructed ESL curves, i.e., Waelbroeck et al. (2002); Bintanja et al. (2005); Rohling et al. (2009); Grant et al. (2014); Spratt and Lisiecki (2016), for their different sea level values during specific periods (e.g., MIS 9e, 7c, 6a, etc. in Fig. 4) and their use on the same type of terrace (e.g., Leclerc & Feuillet, 2019; de Gelder et al., 2023). The resulting best-fit simulations are named W02, B05, R09, G14, and S16 (Fig. 4). We note that ideally GIA-corrected RSL curves should be used that are adjusted to local effects at Cape Laundi, but such curves are currently not available, and given Sumba's far-field location, differences would only be on the order of a few meters. In the following we use ESL when discussing the general characteristics of SL during the different MIS stages and the SL reconstructions used, and RSL when discussing the relative local changes of SL with respect to the Cape Laundi.

The reconstruction of Waelbroeck et al. (2002) is based on oxygen isotopic ratios of benthic foraminifera from the North Atlantic and Equatorial Pacific Ocean over the four last glacial-interglacial cycles (the last 430 ka), calibrated with the elevation of coral samples corrected from vertical deformation. Thus, Waelbroeck et al. (2002) provide the result of a compilation of several proxies from different parts of the global ocean. Bintanja et al. (2005) used numerical modeling to reconstruct ESL variations and continental ice volume over 1 Ma from a continuous global compilation of benthic oxygen isotope data. This ESL curve therefore covers a longer period, ensuring that the entire Cape Laundi sequence is simulated (its age is estimated at 1 Ma; Pirazzoli et al., 1991). We used this curve to complete the others up to 1 Ma. Rohling et al. (2009) used the oxygen isotopic ratios of planktonic foraminifera and bulk sediment from the central Red Sea over 520 ka, while inferring those local variations are roughly representative of ESL. Also in the Red Sea, Grant et al. (2014) used a new chronology derived from a U/Th-dated speleothem oxygen isotopic ratio record and based their approach on the synchronization of an Asian monsoon signal with dust and sea level records, to propose a sea level curve over 500 ka. Lastly, the meta-analysis of Spratt and Lisiecki (2016) is based on a principal component analysis of earlier compilations (Waelbroeck et al., 2002; Bintanja et al., 2005; Sosdian and Rosenthal, 2009; Rohling et al., 2009; Elderfield et al., 2012; Rohling et al., 2014; Shakun et al., 2015), up to 800 ka. As a consequence of the different reconstruction methods, these ESL curves span a range of temporal lengths and resolutions.

We modeled the Cape Laundi sequence with ranges of uplift rates (U: 0.42-0.52 mm a^{-1}, every 0.02 mm a^{-1}), maximum reef growth rates (G_{max}: 6-14 mm a^{-1}, every 2 mm a^{-1}), erosion rates (E: 20-60 mm^3 a^{-1}, every 10 mm^3 a^{-1}), and initial basement slope (α: 5-7 %, every 1 %). The choices of ranges are either restricted because they are justified by previous studies (i.e., U; Pirazzoli et al., 1993; Nexer et al., 2015), they are somewhat restricted by our field observations (i.e., α; observation of the bedrock in the main river bed at Cap Laundi), or they cover a large range because they are not constrained, either by previous studies or by field observations (i.e., E and G_{max}). Concerning the uplift rate, we first conducted several tests with uplift rates ranging from 0.2 mm a^{-1}, as proposed by Bard et al. (1996), to 0.68 mm a^{-1}. The simulations obtained with these rates differed so much from our altimetry measurements and the chronology proposed by previous authors (Pirazzoli et al., 1991; Bard et al., 1996; See (Supplementary Information B05-U0.20-Gmax06-E60-P06 and W02-U0.68-Gmax08-E60-P06), that we chose to restrict our range of values to those above. The maximum and optimal reef growth depths (h_{max} and h_{ow}, respectively) and the maximum depth of wave erosion (h_{wb}) are set to be 20 m (Bosscher and Schlager, 1992), 2 m and 3 m, respectively, based on our field observations of areas with high coral growth (reef crest and fore-reef zones) and wave action at low tide. Each of the 625 simulations is compared to the morphometric data (dGPS and sonar), and radiometric ages (i.e., U/Th- and ESR-dating) for the Cape Laundi sequence (Fig. 5A; Pirazzoli et al., 1993; Bard et al., 1996).

We scored each numerical simulation based on the outcrop of reef construction in agreement with robust ages and 8 morphological criteria: the morphology (i.e., overall shape of the CRT and elevation of surrounding inner edges) of **1)** CRT II$_1$, **2)** CRT I$_2$, **3)** CRT II, **4)** modern reef, **5)** CRT III & CRT IV, **6)** occurrence of two submerged CRTs, **7)** occurrence of a submerged barrier reef, **8)** inner edge of CRT II$_0$ (elevation of ~40 m and only observable on profile 2; Fig. 5A). The overall shape of the CRT was studied manually by comparing the measured topographic profile (Fig. 5A) with the simulated one. The simulated inner edges were also manually selected by choosing the steepest break in slope. These were then compared with those measured with dGPS data (Fig. 5). The two submerged CRTs correspond to CRTs -I (also corresponding to the submerged barrier reef) and -II visible in Fig. 5. We consider here that a barrier reef is a reef with an inner lagoon several meters deep (e.g., Kennedy et al., 2021), as opposed to fringing reefs characterized, among others, by an inner reef flat 1 or 2 meters deep.

For each criterion, we gave a score out of 5 (with a step of 0.5). Then, we summed up these scores with different weightings for each criterion. Due to a better chronological constraint (the most robust ages are concentrated on the main CRT I) and the particular focus of this study on the morphogenesis of the lower CRTs, a coefficient of 2 was given to criteria **1)** and **2)**. In contrast, because of the significant lateral variation of CRT II_0 and its presence only on topographic profile 2 (Fig. 1B), a coefficient of 0.5 is given to criterion **9)**. In the same vein, the same coefficient is given to critieria **7)** and **8)** as we observed these submerged CRTs and this barrier reef only on one bathymetric profile and therefore we have little constraint as to its lateral variation along the coast. A coefficient of 1 is given to criteria **3)**, **4)** and **5)**. Thus, the maximum score that a simulation can achieve is 42.5.

3.4. Selection of robust dating

We selected U-series ages from previous studies (Pirazzoli et al., 1991, 1993; Bard et al., 1996), requiring **1)** lack of recrystallisation of the primary aragonite (less than 2 % calcite; e.g., Obert et al., 2016), **2)** ^{238}U concentration in the range of modern coral species (2.75 ± 0.55 ppm; e.g., Robinson et al., 2003; Lazar et al., 2004; Scholz et al., 2004), **3)** low values of ^{232}Th (< 0.0004 ppm) and high values of $^{230}Th/^{232}Th$ (> 200; e.g., Scholz et al., 2004), and **4)** $^{234}U/^{238}U$ values which, combined with apparent $^{230}Th/^{234}U$ ages, give back-calculated initial $^{234}U/^{238}U$ values that are in the range of modern seawater: $\delta^{234}U_i$ = 140-152 ‰; Chutcharavan and Dutton, 2021);). We chose a relatively wide range of values for the $\delta^{234}U_i$ because the average $\delta^{234}U_{seawater}$ value for previous interglacials (e.g., MIS 5e) is not constrained. In addition, the uranium isotopic composition of sea water has varied by several per mil during glacial–interglacial cycles (Chen et al., 2016; Chutcharavan et al., 2018).

We retained only 4 ages out of 31 U-series Pleistocene ages. These four ages (samples SBA 9, 10, 12, and 14 in Bard et al., 1996 and in bold in Figs. 1 and 5A; Table 2) are therefore the most robust Pleistocene ages obtained at Cape Laundi. The very low number of dating that pass our criteria is mainly due to the fact that **1)** Pirazzoli et al. (1991, 1993) did not provide all the information listed in our criteria, so we cannot determine the robustness of their dating, and that **2)** the $\delta^{234}U_i$ values given by Bard et al., (1996) are almost all higher than 155 ‰, testifying to the open-system behavior of corals and the post-depositional diagenetic effects that affected them (e.g., Obert et al., 2016). Furthermore, given the large uncertainties in the previous ESR dating (Pirazzoli et al., 1991, 1993), we do not consider these ages as a robust chronological constraint. However, given the lack of ages passing our criteria, we will use the other dates to compare and discuss our results but with less confidence. From now on, when the two robust dates are used, they will be referred to by the acronym MRD (i.e, Most Robust Dating).

Samples	CRT	Elevation	Species	Calcite	^{238}U	$^{230}Th/^{234}U$	$^{234}U/^{238}U$	Age	⍰$^{234}U_{initial}$
		m	in situ	%	ppm	± 2σ	± 2σ	ka ± 2σ	± 2σ
SBA 9	I1	3	*Diploastrea heliopora*	0	2.42	0.712 ± 0.003	1.105 ± 0.002	131.2 ± 1.0	152 ± 4
SBA 10	I1	3	*Goniastrea*	0	2.56	0.553 ± 0.002	1.114 ± 0.003	86.0 ± 0.6	146 ± 4
SBA 12	I1	3	*Porites* (micro-atoll)	0	2.57	0.637 ± 0.002	1.113 ± 0.002	107.6 ± 0.7	154 ± 3
SBA 14	I2 ?	3	*Favia stelligera*	0	2.68	0.676 ± 0.003	1.111 ± 0.003	119.3 ± 1.0	156 ± 5

Table 2. Most robust dating selected for Cap Laundi. All the information in this table come from Bard et al (1996). Elevations are relative to the present mean low water spring level and have been rounded to the nearest meters. Sample SBA 14 was reported on CRT I_2 by Bard et al. (1996), but given its location away from the other samples (i.e., north of Cap Laundi; Fig. 1) and its identical elevation to samples taken on CRT I_1 (i.e., 3 m relative to the present mean low water spring level), we are unable to determine whether it was actually sampled on CRT I_1 or I_2. The age from this sample is therefore placed on CRT I_1 in Fig. 5 and the figures in the supplementary information.

4. Results

Here we detail the results from the model used (i.e., Pastier et al., 2019), **1)** showing the parameter ranges obtained for the best-fit simulations (i.e., B05, W02, R09, G14, S16; Fig. 6), then **2)** comparing the best-fit simulation obtained (i.e., B05) with the field measurements data (Fig. 7) and the chronological constraints for the whole sequence (Table 3), and **3)** comparing the other best-fit simulations (i.e, W02, R09, G14, S16) with the same data but only for the lower part of the Cape Laundi sequence.

4.1. CRTs sequence at Cape Laundi

Resulting scores are given in Fig. 6. We identified clusters of good scores and selected the best-fit simulation for each ESL curve (Fig. 6). High score simulations are obtained with **1)** uplift rates (U) ranging between 0.45 mm a^{-1} (W02 and S16), 0.46 mm a^{-1} (R09), and 0.50 mm a^{-1} (B05 and G14), in line with the upper values but not at all with the lower values of previous studies (Pirazzoli et al., 1993; Bard et al., 1996; Nexer et al., 2015), **2)** a maximum reef growth rate (G_{max}) of 6 mm a^{-1}, corresponding to an effective reef growth rate of about 4 mm a^{-1} (section 3.3.), **3)** an erosion rate (E) of 60 mm^3 a^{-1}, and **4)** an initial slope (ɑ) of 6-7 % (Fig. 6). Therefore, despite the differences between the ESL reconstructions used (Fig. 4), the best-fit simulations selected constrain the sequence morphogenesis parameters over similar parametric ranges.

4.2. The best-fit simulation for Cape Laundi

The highest score simulation (i.e., 30.5; Fig. 6) is obtained with the ESL curve of Bintanja et al. (2005). It most accurately predicts the morphology of the lower CRTs of the sequence (i.e., the CRTs below CRT III; Fig. 7) and to the roundness of the distal edges of CRTs (Fig. 5). Thus, to improve the interpretation of the CRTs sequence, we studied **1)** the spatial differences between B05 (U: 0.50 mm a^{-1}; G_{max}: 6 mm a^{-1}; E: 60 mm^3 a^{-1}; α: 6 %) and our field measurements (Fig. 7), and **2)** the temporal differences between the chronological constraints derived from this simulation and previous dating (Pirazzoli et al., 1991, 1993; Bard et al., 1996; See Section 2).

Nomenclature of the CRTs	MIS associated with CRTs (from Best-fit simulation, B05)	Elevation of CRTs		Width of CRTs	
		Altimetric measurements (Elevation of inner edge ; dGPS ; m)	Best-fit simulation (Elevation of inner edge; ± 1 m)	Altimetric measurements (dGPS ; ± 1 m)	Best-fit simulation (± 1 m)
CRT	MIS 1	0 ± 0.5	0	288	359
CRT I1	MIS 1 ; 5a ; 5c	6.4 ± 0.5	12	182	313
CRT I2	MIS 5c ; 5e	23.2 ± 0.5	19	484	242
CRT II0	MIS 5e	42.4 ± 0.5			
CRT II1	MIS 5e	57.1 ± 0.5	63	251	399
CRT II2	MIS 5e ; 7a ; 7c	76.0 ± 0.5	78	218	261
CRT II3	MIS 7c ; 7e	79.9 ± 0.5	86	73	207
CRT II4		95.0 ± 0.5	100	312	141
CRT II5	MIS 9a ; 9c/e	105.4 ± 0.5	101	135	259

CRT II6		119.3 ± 0.5	123	367	190
CRT II7	MIS 9c/e	136.6 ± 0.5	137	312	305
CRT III	MIS 11	165.4 ± 0.5	163	293	457
CRT IV	MIS 13	250.5 ± 1.5	248	1514	1426
CRT V	MIS 15 ; 17	341.0 ± 1.5	324	1086	1434
CRT VI	MIS 19 ; 21 ; 23	389.3 ± 1.5	413	279	1567
CRT VII	MIS 25 ; 27 ; 29	470 ± 1.5			

Table 3. Nomenclature (from this study), associated MIS inferred from B05, elevation, width of CRTs from dGPS field measurements and the best-fit simulation (i.e., B05). For best-fit simulation columns, ± 1 m corresponds to the spatial resolution of the model. For CRT widths, ± 1 m corresponds to the resolution of the Pleiades images (from which the DEM is derived), as these measurements were double-checked with these satellite images and the dGPS profile.

CRT I_1 has a measured width of 180 m and an inner edge raised at 6.4 ± 0.5 m (Fig. 5A) whereas its simulated width amounts to 313 m and its inner edge elevation lies at 12 m (Figs. 5B, 7A). If we consider only robust datings (see section 3.4.; Table 2; Fig 5A), CRT I_1 ages range from 2 ka to 131 ka. B05 also suggests that this CRT is composite, but with predicted ages of MIS 5c and 5a (Fig. 5B). CRT I_2 is 484 m wide, and its inner edge is found at 23 m (Fig. 5A). The simulation suggests a width half that of the measured one and an elevation of the inner edge of 19 m (Fig. 5B; Table 3). On this CRT, coral colonies have been dated from 93 ± 14 ka to 142 ± 21 ka by Pirazzoli et al. (1993) and from 93.4 ± 0.6 ka to 135.7 ± 1.3 ka by Bard et al. (1996). The simulation proposes an age correlated with MIS 5e (116 to 128 ka; Fig. 5B).

The simulated CRT II_1 has a maximum elevation of 63 m and a width of ~400 m; field measurements yield 57 m and 251 m respectively (Table 1; Fig. 5). Pirazzoli et al. (1993) obtained ages ranging from 117 ± 18 ka to 275 ± 41 ka from coral colonies sampled on the CRT surface. The only robust age of this CRT is 129.9 ± 0.9 ka (Bard et al., 1996). The best-fit simulation suggests a reef construction during MIS 5e (Fig. 5B). CRT II_2 has a width of 218 m and a maximum elevation of 76 m (Table 3; Fig. 5A). The simulation width and elevation of this CRT are 261 m and 78 m, respectively (Table 3). The coral colonies dated on this CRT show very heterogeneous ages, ranging from 140.8 ± 1.3 ka to 356 ± 10 ka (Fig. 5A), leading to a possible correlation of the CRT with MIS 6 as well as with MIS 11. For CRT $II_{2,}$ the simulation suggests ages between 118.5 and 226.5 ka, which suggests possible correlation with MIS 5e, MIS 7a and MIS 7c. In the field, CRT II_3 has a narrow width of 73 m and a maximum elevation of 80 m (Table 3). In the simulation, it reaches a width of 207 m and an elevation of 86 m. The simulated surface of CRT II$_3$ does not match the overall shape observed in the field (Fig. 5). In addition, there are no chrono-stratigraphic constraints for the RLUs forming CRT II$_3$ (Fig. 5A). Simulations suggests a possible correlation with MIS 7c (Fig. 5B). CRT II$_4$ is 312 m wide and has a maximum elevation of 95 m in the field (Table 3). The simulation does not suggest any terrace (Fig. 5B). Again, there is no age chrono-stratigraphic constraints for RLUs composing this CRT. However, the simulation gives a correlation with MIS 7e (Fig. 5B). In the field and in the simulation, CRT II$_5$ has a width of 135 m and 259 m and an inner edge elevation of 105.4 ± 0.5 m and 101 m, respectively (Table 3). For the RLUs forming CRT II$_5$, the simulation suggests an age between 279.5 and 298.5 ka (i.e., corresponding to MIS 9a; Fig. 5B).

The simulation highlights an elevation and width of 123 m and 190 m for CRT II$_6$, where the field measurements show 119 m and 367 m, respectively (Table 3). For this CRT, the simulation suggests an age ranging between 298.5 and 337.5 ka associated to MIS 9e/c. CRT II$_7$ reaches a maximum elevation of 137 m, both by the field measurements and the simulation (Table 3; Fig. 5). The width of this CRT is measured at 312 m and 305 m with the dGPS and the simulation, respectively (Table 3). The simulation also suggests an age correlated to MIS 9c/a for this CRT. CRT III has a measured width of 293 m (457 m with the simulation) and an inner edge elevation found at 165 m (163 m with the simulation; Table 3). Three ages were previously obtained for this CRT: 322 ± 48, 327 ± 49 and 397 ± 59 ka (Fig. 5A; Pirazzoli et al., 1993). The simulation suggests a correlation with MIS 9e/c. Thus, the results of the present study highlight the possible formation of three distinct CRTs (II_6, II_7 and III) during MIS 9e/c.

The stacked swath profiles (Fig. 3) reveal the lateral morphological variability of the upper CRTs: some intermediate CRTs are not present laterally at Cape Laundi. Moreover, besides two ages with large uncertainties (i.e., 584 ± 88 and 603 ± 90 ka on the distal edge of CRT V; Pirazzoli et al., 1993) no age constraint exist on CRT IV, which does not help interpreting our simulations. Nevertheless, the simulation successfully reprocesses the morphometric observations related to CRT IV (CRT width and inner edge elevation; Table 3; Fig. 7). More precisely, the measured width and elevation are 1514 m and 251 m, where the simulation predicts 1426 and 248 m (Table 3). The distal edge of this CRT has a simulated age ranging from 358.5 to 425 ka. We suggest a correlation with MIS 11 in conformity with previous studies (Nexer et al., 2015). For the upper part of the Cape Laundi sequence, the discrepancy between the simulation and field observations become more prominent (Table 3; Fig. 7). For example, the inner edges of CRTs V and VI are measured in the field at 341 and 389 m, where the simulation yielded 324 and 413 m (Table 3). The same applies to the widths of these two CRTs, which are measured at 1086 m and 279 m, whereas the simulation gives widths of 1434 and 1567 m (Table 3). Concerning the age estimations of these CRTs, our results are in agreement with previous studies (i.e., correlation from MIS 15 to MIS 23; Fig. 5; Pirazzoli et al., 1993). Finally, concerning the highest CRT of Cape Laundi (VII), our simulation suggests an elevation of 470 m (such as our field measurements; Fig. 5) and an age of formation at MIS 29, 27 and 25, in agreement with earlier studies (Pirazzoli et al., 1993).

4.3. Comparison of the modeled lower part of the sequence obtained with the different simulations

Here the results of the simulations (other than B05) are presented for the lower part of the sequence (i.e., main CRT II and I; the full best-fit simulations are available in the supplementary data, as well as the animations for each best-fit simulation).

The simulated morphology of the main CRT II with W02 (U: 0.45 mm a^{-1}; G_{max}: 6 mm a^{-1}; E: 60 mm^3 a^{-1}; α: 6 %; Fig. 8A) is relatively consistent with our measurements (Fig. 5A). In addition, this simulation predicts a CRT that is only present on dGPS profile 2 (CRT II_0; Figs. 5A; 8A). However, no RLU related to MIS 5e is simulated on CRT I_1 and I_2, which is at odds with previous work (Pirazzoli et al., 1993; Bard et al., 1996). Finally, W02 suggests the initiation of a Holocene drowned barrier reef as observed offshore Cape Laundi (Figs. 5A; 8A; Chauveau et al., 2021b).

R09 (U: 0.46 mm a^{-1}; G_{max}: 6 mm a^{-1}; E: 60 mm^3 a^{-1}; α: 6 %) also show this submerged barrier reef (Fig. 8B). This simulation predicts a 136 m wide Holocene CRT raised at 3.5 m above msl. This result can be explained by the high frequency of this ESL curve (Fig. 4). Then, the simulated main CRT I has a morphology close to the observed one. However, this simulation shows mainly outcropping RLU associated with MIS 5c (Fig. 8B). Some outcrops of RLUs related to MIS 5a and 5e are obtained on CRT I_1 and at inner edge of CRT I_2, respectively (Fig. 8B). As observed in the field, the simulated morphology of the intermediate CRTs of the main CRT II is characterized by weakly sloping distal parts (Fig. 8B).

G14 (U: 0.50 mm a^{-1}; G_{max}: 6 mm a^{-1}; V: 60 mm^3 a^{-1}; α: 7 %) predicts a submerged barrier reef (Fig. 8C). This simulation shows a main CRT I mainly constructed by a RLU associated with MIS 5c, only few parts of MIS 5e and 5a RLUs outcrop. The simulated morphology of the main CRT II is globally in disagreement with field measurements. For example, the simulated CRT II_3 has a very "rectangular" shape and a width of more than 500 m, where field measurements show a rounded morphology and a width of a few tens of meters (Figs. 5A; 8C).

With S16 (U: 0.45 mm a^{-1}; G_{max}: 6 mm a^{-1}; E: 60 mm^3 a^{-1}; α: 6 %), we found a morphology of main CRT II more in line with morphometric measurements (Figs. 5A; 8D). However, no RLU associated with MIS 5e is outcropping on the main CRT I, only two RLUs associated with MIS 5c and MIS 5a (Fig. 8D). Also, this simulation does not show any submerged barrier reef, but two submerged CRTs now. The model predictions obtained with W02, R09, and G14 suggest a CRT at about 40 m (II_0 on profile 2; Figs. 5A; 8A, 8B, 8C), while B05 and S16 fail to reproduce it (Figs. 5B; 8D).

Finally, using a constant uplift rate (from 0.45 to 0.5 mm a^{-1}) throughout and including substantial wave erosion rates (Section 3.3.), the models used herein successfully predict both the age range and morphology of the highest CRT VII (~470 m) at about 1 Ma (as suggested by Pirazzoli et al., 1993) as well as the lower CRTs (below CRT II_1, in agreement with the dating and topographic measurements; Fig. 5). This encourages us to explore in more detail how the morphogenesis of diachronic lower terraces may be explained without invoking any uplift rate variations (as in Bard et al., 1996).

5. Discussion

Here we discuss, **1)** the model's limitations and behavior, **2)** the scenario to explain the presence of several MIS 5e records at Cape Laundi, **3)** the reoccupation of the lowermost main CRT during MIS 5c and 5a, and finally **4)** discuss the interactions between reef construction and RSL fluctuations on the final morphology of the CRTs.

5.1. Model limitations and behavior

The use of models makes it possible to discuss and better constrain the influence of processes involved in the morphogenesis of terrace sequences (e.g., Matsumoto et al., 2022). However, it is important to note the limitations of the model, which can lead to discrepancies between the model's predictions and the actual morphology of the studied sequence. Firstly, we implemented here a constant uplift rate (U) over 1 Ma, while it is possible that it varied slightly over this period (e.g., Pirazzoli et al., 1991, 1993; Bard et al., 1996). Given that the robust age controls are concentrated solely on CRT I and have a maximum of 131.2 ± 1.0 ka (MRD; associated with MIS 5e), it is possible to assert that there was a constant rate of uplift up to MIS 5c-5e, but this does not preclude a variable rate before this period. Secondly, the marine erosion (E) calculated here is based on the wave erosion model of Anderson et al. (1999), basically representing exponential wave force decay with distance (or decreasing depth), while most recent rock coast studies show much more complicated wave transformations across platforms (e.g., considering the influence of infragravity waves on cliff retreat; Dickson et al. 2013). Thirdly, we assume a linear initial basement slope (α), whereas it is highly unlikely that terraced landscapes begin with a linear topography. Fourthly, the model does not take into account subaerial erosion, although the importance of this has been demonstrated at Cap Laundi (Chauveau et al., 2021b). Finally, the model used here does not consider the uncertainty of the SL curves, which can amount to ±12 m for Bintanja et al. (2005) or ±13 m for Waelbroeck et al. (2002).

Despite these limitations, the model is able to faithfully reproduce the overall morphology of the Cap Laundi sequence (Figs. 5; 7; 8). The clusters of good scores (Fig. 6) show that the set of best-fit simulations are those with the same values of maximum reef growth rate (G_{max} = 6 mm a^{-1}) and marine erosion rate (E = 60 mm^3 a^{-1}). This observation may call into question the fact that the value ranges used in this study are quite broad. However, we highlight that with G_{max} values > 6 mm a^{-1}, built-up reefs quickly fill up their accommodation space, forming rectangular CRTs, in contrast to the rounded morphology observed in the field (Fig. 5A), and preventing reoccupation during subsequent SL highstands (see Supplementary Information-B05-U0.50-Gmax14-E60-P06 and Section 5.4. for more information about the influence of the accommodation space on reef constructions). A simulated rectangular morphology was also found with values of G_{max} = 6 mm a^{-1} and E = 20 mm^3 a^{-1} (see Supplementary Information-B05-U0.20-Gmax06-E20-P06). Thus, there appears to be a close relationship between the maximum reef growth rate and the marine erosion rate: the higher the maximum reef growth rate, the higher the marine erosion rate should be to accurately simulate the morphology of the Cap Laundi sequence, and vice versa. In fact, marine erosion and clastic sedimentation serves to spatially limit reef growth (and especially limits barrier development, as deduced by Pastier et al., 2019) and will, in addition to the relationship between the reef growth rate and the rate of RSL change discussed in Section 5.4, promote the formation of the rounded shape of the CRTs distal edges at Cape Laundi. Moreover, these two parameters favor the genesis of composite CRTs, as deduced in previous studies (Pirazzoli et al., 1991, 1993; Pastier et al., 2019; Chauveau et al., 2021b). Thus, the interplay between reef growth, coastal erosion and sediment accumulation is very important in the morphogenesis of the Cape Laundi coastal sequence, as previously noticed (Chauveau et al., 2021b).

5.2. Scenario for multiple records of MIS 5e

Most of the best-fit simulations (all except S16) suggest at least two CRTs created during MIS 5e and not necessarily during the peak of the ESL highstand (Figs. 5B; 7). Several inner edges for unique ESL highstands could have formed because **1)** ESL during this MIS had several peaks (e.g., Rohling et al., 2009), as inferred from several CRT sequences showing double/multiple CRTs associated with MIS 5e (e.g., O'Leary et al., 2013) or **2)** morphogenetic processes and pre-existed CRTs have influenced the formation of younger reef constructions.

Whether ESL curves show multiple peaks (Rohling et al., 2009) or one peak (Waelbroeck et al., 2002; Bintanja et al., 2005; Grant et al., 2014) during MIS 5e (Fig. 4), most of the simulations obtained show at least two CRTs associated with MIS 5e (Figs. 5B; 8). This seems to indicate that multiple ESL or RSL peaks are not required to explain the presence of several CRTs associated with MIS 5e at Cape Laundi. Instead, we propose that the most likely explanation is the influence of antecedent RLUs on the new ones; here, the fossil RLUs of MIS 6/7.

We unravel the development of successive RLUs from B05 by looking at individual time slices of a typical model run (Fig. 9). At 130 ka, the highest CRT of the MIS 6 was first reoccupied by a reef of a few meters thick (Figs. 9A, 9B). This new reef was then flooded during the transgression of MIS 5e (Fig. 9C). Up to 125 ka (towards the end of MIS 5e transgression), the sea slightly eroded the large cliff associated with MIS 7 and thin layer of corals grew on the fossil sea cliff (Fig. 9C). This was followed by the MIS 5e ESL highstand, during which a reef expanded on the previous MIS 7 RLUs (Fig. 9D). The MIS 5e/5d regression started at 117 ka (e.g., Rovere et al., 2016b), eroded, and slightly reoccupied the MIS 5e RLUs constructed on the paleo-cliff of MIS 7 (Fig. 9E). We interpret this SL regression episode as responsible for the formation of CRT II$_0$ (as also suggested by W02, R09, and G14; Figs. 8A, 8B, 8C). At 113 ka, RSL declined to the depth of the first MIS 5e RLU, itself built on the antecedent RLUs of MIS 6 (Fig. 9F). This was followed by MIS 5d SL lowstand and associated RLUs on the antecedent MIS 6 constructions.

This scenario explains the conflicting ages on the lowermost main CRT I. On CRT I_1, corals have been dated at 131.5 ± 1.0, 131.2 ± 1.0 (MRD), and 130.0 ± 1.2 ka (Bard et al., 1996; Fig. 5), indicating a reefal construction during the MIS 5e transgression. On CRT I_2, corals were dated at 125.2 ± 0.9 and 124.8 ± 0.9 ka, indicating a more recent reoccupation of the foundations. Alternatively, the occurrence of MIS 5e age on CRT I_1 could also be explained by eroded and reworked MIS 5e material during MIS 5e ESL regression or more recent ESL highstands (i.e., MIS 5c and 5a). Our scenario also agrees with the only robust age constraint obtained on II_1 (i.e., 129 ± 0.9 ka; Bard et al., 1996). Ages of 117.8 ± 1, 113.2 ± 0.9, or 119.3 ± 1 ka (MRD), were obtained with coral colonies scattered over the main CRT I (Pirazzoli et al., 1993; Bard et al., 1996). These dates indicate a reshaping and reoccupation of MIS 5e transgressive RLU during MIS 5e regression.

Here, we provide an alternative scenario to the commonly used bijective approach, wherein a ESL or RSL highstand is reciprocally linked to a coastal terrace (see Pastier et al., 2019). We show instead that a single MIS can create several CRTs (as described in Barbados or in Western Australia for example; for more details, see Hearty et al., 2007) and be responsible for diachronic ages on the same CRT. This is mainly explained by the presence of antecedent CRTs which influence the new reef constructions. Furthermore, we underline the importance of the entire SL history in the generation of a CRT, and not just the highstands.

5.3. Reoccupation during MIS 5c and 5a

Here, thanks to the different SL curves used in this study and comparing our results with previous studies (Pirazzoli et al., 1993; Bard et al., 1996; Chauveau et al., 2021b), we discuss the influence of MIS 5c and 5a in the morphogenesis of main CRT I.

B05 does not suggest constructive reoccupation of CRT I_2 (which is associated with the RSL transgression and regression of MIS 5e) during MIS 5c and 5a (Figs. 9G, 9H), but show a partial reoccupation of the CRT associated with MIS 5c (i.e., the most landward part of the actual CRT I_1) during MIS 5a (i.e., CRT I_1 on Fig. 5B; Fig. 9G). In contrast, on main CRT I (including CRT I_1 and I_2; see Fig. 5A), the model highlights three inner edges, elevated at 22, 13, and 3 m, respectively associated with MIS 5e, 5c, and 5a (Fig. 5B). Field observations show two inner edges raised at 23.2 m (CRT I_2) and 6.3 m (CRT I_1). Coral-colonies sampled on the CRT I_2 surface were dated at 93 ± 13 ka (Pirazzoli et al., 1993) and 93.4 ± 0.6 (Bard et al., 1996) and correlate with MIS 5c. On CRT I_1 coral colonies provided ages of 82 ± 4 (Pirazzoli et al., 1993), 86 ± 0.6 (MRD), and 107.6 ± 0.7 ka (MRD; Bard et al., 1996), which lead to the interpretation that this CRT was built during MIS 5c and MIS 5a. Thus, contrary to what B05 suggests, the MIS 5c and 5a RSL highstands have built RLUs now above 13 m and 3 m, respectively. These simulated low elevations can be explained by the fact that the ESL of MIS 5a and 5c proposed by Bintanja et al. (2005) are lower than other ESL curves (e.g., W02; G14; S16; Fig. 4). Besides, most simulations show a full reoccupation of the main CRT I (CRT I_1 and I_2) during MIS 5c and 5a (Figs. 8A, 8B, 8C, 8D).

Considering a constant uplift of 0.5 mm a^{-1} and using recent ESL estimates of -11.1 ± 6.6 m and -10.5 ± 5.5 m for MIS 5c and 5a (which are higher than the estimates of SL curves used as model input; Creveling et al., 2017) would lead to theoretical inner edge elevations of 39 ± 8 m and 31 ± 7 m, respectively. Thus, MIS 5c and 5a highstands could have reoccupied the entire surface of the lowermost main CRT (I). This hypothesis could explain **1)** the corals dated as MIS 5c on the CRT I_2 and MIS 5c and 5a on the CRT I_1 (Pirazzoli et al., 1993; Bard et al., 1996) and **2)** the homogeneous ^{36}Cl cosmogenic concentrations measured for the whole CRT (Chauveau et al., 2021b), interpreted as a final abandonment of the surface during a single event (i.e., MIS 5c or 5a). Indeed, the interaction of secondary cosmic rays with rocks exposed in the Earth's surface produces cosmogenic isotopes (e.g., Gosse and Phillips, 2001). The abundance of these isotopes increases with exposure time until steady state, when production and decay of the cosmogenic isotope are balanced (e.g., Schlagenhauf et al., 2010). The homogeneity of the ^{36}Cl concentrations measured on the main CRT I (see Table 2 in Chauveau et al., 2021b) is therefore evidence of the formation of the upper reefal limestone unit (forming CRT I_1 and I_2) during a single sea level highstand.

5.4. Explanation of the sequence morphology

Here, we focus on **1)** the rounded distal edges of CRTs, **2)** the influence of the accommodation space on reef constructions during RSL transgressions, highstands and regressions, **3)** the role of antecedent RLUs on the accommodation space, and more broadly **4)** interplay between reef growth and RSL changes.

The rounded shape of the CRTs distal edges leads to subtle slope dip changes between adjacent CRTs and mild inner edges. We successfully reproduce these landforms in our best-fit simulation (i.e., B05; Fig. 5B), as well as in W02 (Fig. 8A) and S16 (Fig. 8D). In contrast, simulations partially fail to reproduce them with G14 (Fig. 8C) and, to a lesser extent, with R09 (Fig. 8B; see explanations below). We also partly reproduce the morphological differences between the main CRTs clearly separated by high and steep distal parts and more subtle intermediate CRTs, especially regarding CRT I and CRT II (Figs. 5A; 8A, 8B, 8D). Main CRT II is a good example of this CRT morphology characterized by low sloping distal parts (Fig. 5A) forming a cluster of subtle terraces. This is best reproduced with W02 (Fig. 8A), as well as B05 (Fig. 5B) and S16 (Fig. 8D), poorly reproduced in R09 and not reproduced in G14.

Our results suggest that the overall rounded shape of individual CRTs is due to the low reef growth rate relative to the rate of RSL change. Indeed, fast growing reefs (G_{max} > 10 mm a^{-1} in our model) entirely saturate their accommodation space, thereby forming “rectangular” CRT distal edges, and steeper cliffs. In this case, the accommodation space is the main limiting factor acting on CRT morphology (Pastier et al., 2019). In contrast, due to the low reef growth rate in our best-fit simulations for each ESL reconstructions, reef growth is typically not limited by its accommodation space, neither for backstepping and catch-up during RSL rise, nor for keep-up and progradation during a RSL highstand (see definitions in Neumann (1985) and in Camoin and Webster (2015)). Indeed, during most transgressions, the low reef growth rate is outpaced by the rate of RSL rise, leading to backstepping and drowning of the reef (as the transgression of MIS 9a for CRT II_6 in W02; Figs. 4; 7A). The duration of RSL highstands does not allow the reef to entirely fill its accommodation space and form large and flat platforms. Consequently, accommodation space is still available for significant reef construction during regressions, unlike fast growing reefs which mainly expand during transgressions (Husson et al., 2018). Construction during RSL fall leads to seaward sloping CRTs surfaces (e.g., CRT II_1, II_3, II_4, II_5, II_6 in Fig. 5A), particularly well expressed in B05 (Fig. 5B), S16, W02, and R09, but not in G14 (Fig. 8). Thus, the absence of clearly marked fossil sea-cliffs and notches in the distal part of most of the CRTs in the Cape Laundi sequence, but also their roundness, is plausible evidence of a last episode of construction during RSL regression.

Reef construction during reoccupations of antecedent RLUs associated with MIS highstands may cover the shoreline angle of antecedent CRTs, leading to missing terraces (e.g., CRT II_4 in Fig. 8C). But these antecedent CRTs also provide the reef with a larger accommodation space, which fosters the development of large and flat CRTs. For example, in our study, ESL reconstructions providing higher elevations for MIS 7c highstand relative to MIS 7a (i.e., W02, B05, and S16) show more realistic morphologies (compared with our dGPS measurements; Figs. 5; 7) than ESL reconstructions with lower relative elevation for the MIS 7c highstand (R09 and G14). With G14 (Fig. 8C), the multiple reoccupations of RLUs constructed during MIS 8, 7e and 7c lead to the formation of the widest and flattest CRT of the sequence (~514 m, CRT II_3 in Fig. 8C). Similarly, the relatively high SL of MIS 9a in the ESL reconstruction of Waelbroeck et al. (2002) (Fig. 4) prevents any reoccupation on CRT II_6 during MIS 7e (Fig. 8A), despite the slightly lower uplift rate (Fig. 6). Both R09 and G14 exhibit a greater difference between the elevations of these highstands compared to that of W02. This greater difference in elevation leads to the coincidence of final relative elevation for MIS 9a and MIS 7e, resulting in the formation of a composite but not compound terrace when modeling with R09 (CRT II_5 in Fig. 8B; Fig. 2). G14 does not show such a composite terrace (Fig. 8C). The accommodation space during the MIS 7e final transgression and highstand is very small due to the former construction of RLU during MIS 9a. Thus, reefal construction is limited during MIS 7e, and the RLU associated with this MIS finally eroded during the following regression. This explains why there is no geomorphic record of the MIS 7e highstand within the final sequence of G14 (Fig. 8C and Supplementary Animation S4). Therefore, the rounded morphology of the intermediate CRTs composing the main CRT II can be explained by the relative elevation of the ESL highstands.

The morphology of the seaward part of CRT IV (associated with MIS 11) is successfully reproduced in W02 (Fig. 8A) and B05 (Fig. 5B). In the other simulations, due to steep sea level regressions after MIS 11 (Fig. 4) the distal part of this main CRT is too steep (Figs. 8B, 8C, 8D) and exhibit well individualized terraces (Figs. 8C, 8D) when these regressions are not linear but show slowdowns (see the SL curve of Spratt and Lisiecki, 2016 in Fig. 4). There are also MIS 11 constructions on CRT III, partly for R09 (Fig. 8B) and for the entire CRT with S16 (Fig. 8D). Similarly, the morphology of CRT IV in our simulations would result from the feedback between RSL variations and the low reef growth rate. The rate of RSL rise after 425 ka (Fig. 4) is slightly higher than the effective reef growth rate (see Section 3.3.). This induces a catch-up growth regime (Neumann, 1985), preventing construction along the whole reef flat and resulting in a migration of the reef crest landward (Fig. 8A and Supplementary Animation S2). Then, the long duration of the highstand results in an increased supply of clastic sediments to the forereef slope, smoothing the slope. Finally, because the accommodation space hasn’t been saturated during the previous transgression and highstand, a narrow fringing reef can construct a thin veneer of limestone all along the slow regression, covering the clastic sediments of the forereef slope. Using other ESL reconstructions, the average rates of RSL rise are either low enough to allow the reef to keep-up, and to form a steep forereef slope (Fig. 8B, Supplementary Animation S3; Fig. 8C, Supplementary Animation S4) or too high and lead to the backstepping of the reef (Fig. 8D, Supplementary Animation S5). Then, all ESL reconstructions of MIS 11 used here (Fig. 4) show second order ESL rises or ESL stagnations, which carve and steepen up the distal part of CRT IV. This can even lead to the formation of extra terraces on the CRT IV distal part, which may be purely erosive, as in W02, G14 and S16 (Figs. 8A, 8C, 8D).

The discussion above serves to illustrate that specific ESL reconstructions lead to specific morphological features that may, or may not, match with observations and dating of CRTs. In a general sense, this study shows that careful modeling of the morphology of a CRTs sequence permits us to unravel the rates of past SL variations, to better understand the bioconstruction formed during transgressions, highstands and regression, and thus potentially to improve SL reconstructions of these fluctuations. This study only focuses on one site and therefore any inferences on global SL reconstructions may be biased by local peculiarities at Cape Laundi (e.g., erosive and constructive reoccupation processes, Chauveau et al., 2021b), but a similar approach may be applied to other sites with double/multiple CRT outcrops associated with MIS 5e (e.g., Hearty et al., 2007). A comprehensive comparison of several such sequences may eventually lead to improved SL reconstructions on a global level.

6. Conclusions

The long-lasting CRT sequence of Cape Laundi has the potential to serve as a crucial archive for studies of Quaternary sea level oscillations. However, until now, the diachronism and the composite nature of coral reef terraces challenged any bijective, or reciprocal, association of a terrace with a discrete sea level highstand. To address this, on the basis of a chrono-morphological study of 625 simulations from a kinematic model based on reef morphology and testing five sea level curves, we are able to constrain the parameters that generated the sequence (i.e., uplift rate, reef growth rate, erosion rate, and slope of foundations). Furthermore, we explain the presence of MIS 5e ages of corals sampled on three distinct terraces by retracing the eustatic history of this MIS and by demonstrating that it is not necessary to invoke a double sea level peak. We also unravel the formation of composite coral reef terraces by highlighting reoccupation during MIS 5c and 5a. Moreover, we explain the rounded morphology of terrace distal edges at Cape Laundi with the low reef growth rate. Finally, we discuss the interactions between reef construction and relative sea level fluctuations on the final morphology of the terraces. Careful modeling can therefore explain the morphology of a sequence of coral reef terraces and, to a greater extent, discuss precisely the processes that generated it.

References

1. Abdullah, C. I., Rampnoux, J. P., Bellon, H., Maury, R. C., & Soeria-Atmadja, R. (2000). The evolution of Sumba Island (Indonesia) revisited in the light of new data on the geochronology and geochemistry of the magmatic rocks. Journal of Asian Earth Sciences, 18(5), 533-546.

2. Anderson, R. S., Densmore, A. L., & Ellis, M. A. (1999). The generation and degradation of marine terraces. Basin Research, 11(1), 7-20.

3. Armijo, R., Lacassin, R., Coudurier-Curveur, A., & Carrizo, D. (2015). Coupled tectonic evolution of Andean orogeny and global climate. Earth-Science Reviews, 143, 1–35.

4. Authemayou, C., Brocard, G., Delcaillau, B., Molliex, S., Pedoja, K., Husson, L., et al. (2018). Unraveling the roles of asymmetric uplift, normal faulting and groundwater flow to drainage rearrangement in an emerging karstic landscape. Earth Surface Processes and Landforms, 43(9), 1885-1898.

5. Authemayou, C., Pedoja, K., Chauveau, D., Husson, L., Brocard, G., Delcaillau, B., … & Scholz, D. (2022). Deformation and uplift at the transition from oceanic to continental subduction, Sumba Island, Indonesia. Journal of Asian Earth Sciences, 236, 105316.

6. Bard, E., Jouannic, C., Hamelin, B., Pirazzoli, P., Arnold, M., Faure, G., et al. (1996). Pleistocene sea levels and tectonic uplift based on dating of corals from Sumba Island, Indonesia. Geophysical Research Letters, 23(12), 1473-1476.

7. Bintanja, R., Van De Wal, R. S. W., & Oerlemans, J. (2005). Modelled atmospheric temperatures and global sea levels over the past million years. Nature, 437(7055), 125-128.

8. Bosscher, H., & Schlager, W. (1992). Computer simulation of reef growth. Sedimentology, 39(3), 503-512.

9. Boulton, S. J., & Stokes, M. (2018). Which DEM is best for analyzing fluvial landscape development in mountainous terrains?. Geomorphology, 310, 168-187.

10. Cabioch, G. (2011). Emerged reefs. Encyclopedia of Modern Coral Reefs: Structure, Form and Process, 373-380.

11. Camoin, G. F., & Webster, J. M. (2015). Coral reef response to Quaternary sea-level and environmental changes: State of the science. Sedimentology, 62(2), 401-428.

12. Caputo, R. (2007). Sea-level curves: perplexities of an end-user in morphotectonic applications. Global and Planetary Change, 57(3-4), 417-423.

13. Chappell, J. (1974). Geology of coral terraces, Huon Peninsula, New Guinea: a study of Quaternary tectonic movements and sea-level changes. Geological Society of America Bulletin, 85(4), 553-570.

14. Chappell, J. (1980). Coral morphology, diversity and reef growth. Nature, 286(5770), 249-252.

15. Chauveau, D., Authemayou, C., Molliex, S., Godard, V., Benedetti, L., Pedoja, K., … & ASTER Team. (2021a). Eustatic knickpoint dynamics in an uplifting sequence of coral reef terraces, Sumba Island, Indonesia. *Geomorphology*, *393*, 107936.

16. Chauveau, D., Authemayou, C., Pedoja, K., Molliex, S., Husson, L., Scholz, D., … & ASTER Team. (2021b). On the generation and degradation of emerged coral reef terrace sequences: First cosmogenic 36Cl analysis at Cape Laundi, Sumba Island (Indonesia). *Quaternary Science Reviews*, *269*, 107144.

17. Chen, T., Robinson, L. F., Beasley, M. P., Claxton, L. M., Andersen, M. B., Gregoire, L. J., ... & Harpp, K. S. (2016). Ocean mixing and ice-sheet control of seawater 234U/238U during the last deglaciation. Science, 354(6312), 626-629.

18. Chutcharavan, P. M., Dutton, A., & Ellwood, M. J. (2018). Seawater 234U/238U recorded by modern and fossil corals. Geochimica et Cosmochimica Acta, 224, 1-17.

19. Chutcharavan, P. M., & Dutton, A. (2021). A global compilation of U-series-dated fossil coral sea-level indicators for the Last Interglacial period (Marine Isotope Stage 5e). Earth System Science Data, 13(7), 3155-3178.

20. Creveling, J. R., Mitrovica, J. X., Clark, P. U., Waelbroeck, C., & Pico, T. (2017). Predicted bounds on peak global mean sea level during marine isotope stages 5a and 5c. Quaternary Science Reviews, 163, 193-208.

21. Crosby, W. O. (1883). Elevated coral reefs of cuba. Journal of Natural History, 12(70), 283-284.

22. Darwin, C. (1842). The Structure and Distribution of Coral Reefs: Being the First Part of the Geology of the Voyage of the Beagle… During the Years 1832-1836: Smith, Elder.

23. Dickson, M. E., Ogawa, H., Kench, P. S., & Hutchinson, A. (2013). Sea-cliff retreat and shore platform widening: steady-state equilibrium?. Earth surface processes and landforms, 38(9), 1046-1048.

24. de Gelder, G., Jara-Muñoz, J., Melnick, D., Fernández-Blanco, D., Rouby, H., Pedoja, K., Husson, L., Armijo, R., & Lacassin, R. (2020). How do sea-level curves influence modeled marine terrace sequences? Quaternary Science Reviews, 229, 106132.

25. de Gelder, G., Husson, L., Pastier, A. M., Fernández-Blanco, D., Pico, T., Chauveau, D., ... & Pedoja, K. (2022). High interstadial sea levels over the past 420ka from the Huon Peninsula, Papua New Guinea. Communications Earth & Environment, 3(1), 256.

26. De Gelder, G., Solihuddin, T., Utami, D. A., Hendrizan, M., Rachmayani, R., Chauveau, D., ... & Cahyarini, S. Y. (2023). Geodynamic control on Pleistocene coral reef development: insights from northwest

Sumba Island (Indonesia). Earth Surface Processes and Landforms. https://doi.org/10.1002/esp.5643

27. Elderfield, H., Ferretti, P., Greaves, M., Crowhurst, S., McCave, I. N., Hodell, D., et al. (2012). Evolution of ocean temperature and ice volume through the mid-Pleistocene climate transition. Science, 337(6095), 704-709.

28. Fernández-Blanco, D., de Gelder, G., Lacassin, R., & Armijo, R. (2019). Geometry of flexural uplift by continental rifting in Corinth, Greece. Tectonics. https://doi.org/10.1029/2019TC005685

29. Fleury, J.-M., Pubellier, M., & de Urreiztieta, M. (2009). Structural expression of forearc crust uplift due to subducting asperity. Lithos, 113(1-2), 318-330.

30. Fortuin, A. R., Van der Werff, W., & Wensink, H. (1997). Neogene basin history and paleomagnetism of a rifted and inverted forearc region, on-and offshore Sumba, Eastern Indonesia. Journal of Asian Earth Sciences, 15(1), 61-88.

31. Gosse, J. C., & Phillips, F. M. (2001). Terrestrial in situ cosmogenic nuclides: theory and application. Quaternary Science Reviews, 20(14), 1475-1560.

32. Grant, K. M., Rohling, E. J., Ramsey, C. B., Cheng, H., Edwards, R. L., Florindo, F., et al. (2014). Sea-level variability over five glacial cycles. Nature communications, 5(1), 1-9.

33. Haig, D. W. (2012). Palaeobathymetric gradients across Timor during 5.7-3.3 Ma (latest Miocene-Pliocene) and implications for collision uplift. Palaeogeography, Palaeoclimatology, Palaeoecology, 331, 50-59.

34. Hantoro, W. S., Jouannic, C., & Pirazzoli, P. A. (1989). Terrasses coralliennes quaternaires soulevées dans l'île de Sumba (Indonésie). Photo interprétation (Paris), 28(1), 17-34.

35. Hantoro, W. S. (1992). Etude des terrasses récifales Quaternaires soulevées entre le Detroit de la Sonde et l'ile de Timor, Indonésie: mouvements verticaux de la croute terrestre et variations du niveau de la mer.

36. Hearty, P. J., Hollin, J. T., Neumann, A. C., O'Leary, M. J., & McCulloch, M. (2007). Global sea-level fluctuations during the Last Interglaciation (MIS 5e). Quaternary Science Reviews, 26(17-18), 2090-2112.

37. Hinschberger, F., Malod, J.-A., Réhault, J.-P., Villeneuve, M., Royer, J.-Y., & Burhanuddin, S. (2005). Late Cenozoic geodynamic evolution of eastern Indonesia. Tectonophysics, 404(1-2), 91-118.

38. Hume, W. F., & Little, O. H. (1928). Raised beaches and terraces of Egypt. *Union Geograph. Intern., Paris, Rept. Comm. Plio-Pleist. Terraces*, 9-15.

39. Husson, L., Pastier, A.-M., Pedoja, K., Elliot, M., Paillard, D., Authemayou, C., et al. (2018). Reef carbonate productivity during Quaternary sea level oscillations. Geochemistry, Geophysics, Geosystems, 19(4), 1148-1164.

40. Husson, L., Riel, N., Aribowo, S., Authemayou, C., de Gelder, G., Kaus, B. J. P., ... & Sarr, A. C. (2022). Slow geodynamics and fast morphotectonics in the far East Tethys. Geochemistry, Geophysics, Geosystems, 23(1), e2021GC010167.

41. Jouannic, C., Hantoro, W. S., Hoang, C. T., Fournier, M., Lafont, R., & Ichtam, M. L. (1988). Quaternary raised reef terraces at cape Laundi, Sumba, Indonesia: geomorphological analysis and first radiometric Th/U and 14C age determinations. Paper presented at the 6th Proceedings International coral reef symposium.

42. Koelling, M., Webster, J. M., Camoin, G., Iryu, Y., Bard, E., & Seard, C. (2009). SEALEX-Internal reef chronology and virtual drill logs from a spreadsheet-based reef growth model. Global and Planetary Change, 66(1-2), 149-159.

43. Kennedy, E. V., Roelfsema, C. M., Lyons, M. B., Kovacs, E. M., Borrego-Acevedo, R., Roe, M., ... & Tudman, P. (2021). Reef Cover, a coral reef classification for global habitat mapping from remote sensing. *Scientific Data*, *8*(1), 196.

44. Lazar, B., Enmar, R., Schossberger, M., Bar-Matthews, M., Halicz, L., & Stein, M. (2004). Diagenetic effects on the distribution of uranium in live and Holocene corals from the Gulf of Aqaba. *Geochimica et Cosmochimica Acta*, *68*(22), 4583-4593.

45. Leclerc, F., & Feuillet, N. (2019). Quaternary coral reef complexes as powerful markers of long-term subsidence related to deep processes at subduction zones: Insights from Les Saintes (Guadeloupe, French West Indies). Geosphere, 15(4), 983-1007.

46. Matsumoto, H., Young, A. P., & Carilli, J. E. (2022). Modeling the relative influence of environmental controls on marine terrace widths. Geomorphology, 396, 107986.

47. Murray-Wallace, C. V., & Woodroffe, C. D. (2014). Quaternary sea-level changes: a global perspective: Cambridge University Press.

48. Neumann, A. C. (1985). Reef response to sea-level rise: keep-up, catch-up, or give-up. In Proceedings of the fifth international coral reef congress Tahiti, 27 May-1 June 1985 volume 3: Symposia and seminars (A) (pp. 105-110). Antenne Museum-EPHE.

49. Nexer, M., Authemayou, C., Schildgen, T., Hantoro, W. S., Molliex, S., Delcaillau, B., et al. (2015). Evaluation of morphometric proxies for uplift on sequences of coral reef terraces: A case study from Sumba Island (Indonesia). Geomorphology, 241, 145-159.

50. O'Leary, M. J., Hearty, P. J., Thompson, W. G., Raymo, M. E., Mitrovica, J. X., & Webster, J. M. (2013). Ice sheet collapse following a prolonged period of stable sea level during the last interglacial. *Nature Geoscience*, *6*(9), 796-800.

51. Obert, J. C., Scholz, D., Felis, T., Brocas, W. M., Jochum, K. P., & Andreae, M. O. (2016). 230Th/U dating of Last Interglacial brain corals from Bonaire (southern Caribbean) using bulk and theca wall material. Geochimica et Cosmochimica Acta, 178, 20-40.

52. Obert, J. C., Scholz, D., Felis, T., Lippold, J., Jochum, K. P., & Andreae, M. O. (2019). Improved constraints on open-system processes in fossil reef corals by combined Th/U, Pa/U and Ra/Th dating: A case study from Aqaba, Jordan. Geochimica et Cosmochimica Acta, 245, 459-478.

53. Pastier, A.-M., Husson, L., Pedoja, K., Bézos, A., Authemayou, C., Arias-Ruiz, C., et al. (2019). Genesis and Architecture of Sequences of Quaternary Coral Reef Terraces: Insights From Numerical Models. Geochemistry, Geophysics, Geosystems.

54. Pedoja, K., Husson, L., Regard, V., Cobbold, P. R., Ostanciaux, E., Johnson, M. E., et al. (2011). Relative sea-level fall since the last interglacial stage: are coasts uplifting worldwide? Earth-Science Reviews, 108(1-2), 1-15.

55. Pedoja, K., Husson, L., Johnson, M. E., Melnick, D., Witt, C., Pochat, S., et al. (2014). Coastal staircase sequences reflecting sea-level oscillations and tectonic uplift during the Quaternary and Neogene. Earth-Science Reviews, 132, 13-38.

56. Pedoja, K., Husson, L., Bezos, A., Pastier, A.-M., Imran, A. M., Arias-Ruiz, C., et al. (2018). On the long-lasting sequences of coral reef terraces from SE Sulawesi (Indonesia): Distribution, formation, and global significance. Quaternary Science Reviews, 188, 37-57.

57. Peñalver, L., Pedoja, K., Martin-Izquierdo, D., Authemayou, C., Nuñez, A., Chauveau, D., ... & Husson, L. (2021). The Cuban staircase sequences of coral reef and marine terraces: A forgotten masterpiece of the Caribbean geodynamical puzzle. Marine Geology, 440, 106575.

58. Pirazzoli, P. A. (2005). A review of possible eustatic, isostatic and tectonic contributions in eight late-Holocene relative sea-level histories from the Mediterranean area. Quaternary Science Reviews, 24(18-19), 1989-2001.

59. Pirazzoli, P. A., Radtke, U., Hantoro, W. S., Jouannic, C., Hoang, C. T., Causse, C., et al. (1991). Quaternary raised coral-reef terraces on Sumba Island, Indonesia. Science, 252(5014), 1834-1836.

60. Pirazzoli, P. A., Radtke, U., Hantoro, W. S., Jouannic, C., Hoang, C. T., Causse, C., et al. (1993). A one million-year-long sequence of marine terraces on Sumba Island, Indonesia. Marine Geology, 109(3-4), 221-236.

61. Railsback, L. B., Gibbard, P. L., Head, M. J., Voarintsoa, N. R. G., & Toucanne, S. (2015). An optimized scheme of lettered marine isotope substages for the last 1.0 million years, and the climatostratigraphic nature of isotope stages and substages. Quaternary Science Reviews, 111, 94-106.

62. Robinson, L. F., Henderson, G. M., Hall, L., & Matthews, I. (2003, December). Controls on d234U in surface waters of the South Island of New Zealand. In *AGU Fall Meeting Abstracts* (Vol. 2003, pp. V51C-0306).

63. Rohling, E. J., Grant, K., Bolshaw, M., Roberts, A. P., Siddall, M., Hemleben, C., et al. (2009). Antarctic temperature and global sea level closely coupled over the past five glacial cycles. Nature Geoscience, 2(7), 500-504.

64. Rohling, E. J., Foster, G. L., Grant, K. M., Marino, G., Roberts, A. P., Tamisiea, M. E., & Williams, F. (2014). Sea-level and deep-sea-temperature variability over the past 5.3 million years. Nature, 508(7497), 477-482.

65. Rovere, A., Stocchi, P. & Vacchi, M. Eustatic and Relative Sea Level Changes. Curr Clim Change Rep **2**, 221–231 (2016a). https://doi.org/10.1007/s40641-016-0045-7

66. Rovere, A., Raymo, M. E., Vacchi, M., Lorscheid, T., Stocchi, P., Gomez-Pujol, L., et al. (2016b). The analysis of Last Interglacial (MIS 5e) relative sea-level indicators: Reconstructing sea-level in a warmer world. Earth-Science Reviews, 159, 404-427.

67. Rupnik, E., Deseilligny, M. P., Delorme, A., & Klinger, Y. (2016). Refined satellite image orientation in the free open-source photogrammetric tools Apero/Micmac. ISPRS Annals of the Photogrammetry, Remote Sensing and Spatial Information Sciences, 3, 83.

68. Scholz, D., Mangini, A., & Felis, T. (2004). U-series dating of diagenetically altered fossil reef corals. Earth and Planetary Science Letters, 218(1-2), 163-178.

69. Schwartz, M. (2006). Encyclopedia of coastal science: Springer Science & Business Media.

70. Schlagenhauf, A., Gaudemer, Y., Benedetti, L., Manighetti, I., Palumbo, L., Schimmelpfennig, I., ... & Pou, K. (2010). Using in situ Chlorine-36 cosmonuclide to recover past earthquake histories on limestone normal fault scarps: a reappraisal of methodology and interpretations. Geophysical Journal International, 182(1), 36-72.

71. Shakun, J. D., Lea, D. W., Lisiecki, L. E., & Raymo, M. E. (2015). An 800-kyr record of global surface ocean δ18O and implications for ice volume-temperature coupling. Earth and Planetary Science Letters, 426, 58-68.

72. Sosdian, S., & Rosenthal, Y. (2009). Deep-sea temperature and ice volume changes across the Pliocene-Pleistocene climate transitions. Science, 325(5938), 306-310.

73. Speed, R. C., & Cheng, H. (2004). Evolution of marine terraces and sea level in the last interglacial, Cave Hill, Barbados. Geological Society of America Bulletin, 116(1-2), 219-232.

74. Spratt, R. M., & Lisiecki, L. E. (2016). A Late Pleistocene sea level stack. Climate of the Past, 12(4), 1079-1092.

75. Tate, G. W., McQuarrie, N., van Hinsbergen, D. J., Bakker, R. R., Harris, R., Willett, S., ... & Zachariasse, W. J. (2014). Resolving spatial heterogeneities in exhumation and surface uplift in Timor-Leste: Constraints on deformation processes in young orogens. Tectonics, 33(6), 1089-1112.

76. Thompson, W. G., & Goldstein, S. L. (2005). Open-system coral ages reveal persistent suborbital sea-level cycles. Science, 308(5720), 401-404.

77. Toomey, M., Ashton, A. D., & Perron, J. T. (2013). Profiles of ocean island coral reefs controlled by sea-level history and carbonate accumulation rates. Geology, 41(7), 731-734.

78. Turcotte, D. L., & Bernthal, M. J. (1984). Synthetic coral-reef terraces and variations of Quaternary sea level. Earth and Planetary Science Letters, 70(1), 121-128.

79. Waelbroeck, C., Labeyrie, L., Michel, E., Duplessy, J. C., McManus, J. F., Lambeck, K., et al. (2002). Sea-level and deep water temperature changes derived from benthic foraminifera isotopic records. Quaternary Science Reviews, 21(1-3), 295-305.

80. Webster, J. M., Wallace, L. M., Clague, D. A., & Braga, J. C. (2007). Numerical modeling of the growth and drowning of Hawaiian coral reefs during the last two glacial cycles (0-250 kyr). Geochemistry, Geophysics, Geosystems, 8(3).

Figure captions

Fig. 1. A) Altimetry map of Southeast Indonesia and location of Sumba Island and Cape Laundi (red square). Elevation data from the Shuttle Radar Topography Mission (SRTM), and bathymetry data from the General Bathymetric

Chart of Oceans (GEBCO), both at 90 m resolution. **B)** Slope map of Cape Laundi from Pleiades satellite imagery. Contours delineate the inner edges of the CRTs, and we indicate the location of previously dated samples (U/Th and Electron Spin Resonance dating; Pirazzoli et al., 1991, 1993; Bard et al., 1996). The most robust dating correspond to those selected in section 3.4.. Several dates are sometimes present in a single box because the dating samples were very close to each other (see Fig. 1 in Bard et al., 1996 and Fig. 2 in Pirazzoli et al., 1993). Some blue stars have no associated dating because this is not specified in the study of Pirazzoli et al. (1993). The light blue dotted line and the pink line indicate topographic (dGPS) and bathymetric (sonar) profile, respectively.

Fig. 2. Sketch of a sequence of coral reef terraces (CRTs), modified from Pedoja et al. (2018), highlighting a high variability of sequence morphology that can occur for a uniform uplift. The inner edges of the main CRT I and CRT II are continuous from the bay to the cape, the inner edges of the CRT I_1 and CRT II_1 are not. Depending on the location along the coast (Bay or Cape), the main CRT II is either compound, i.e., consisting of two CRTs (i.e., CRT II_1 et II_2) but a single reefal limestone unit (i.e., RLU III; Profile 1), or composite, i.e., consisting of a single CRT (i.e., CRT II) but including several RLUs (i.e., RLU III and IV; Profile 2). The RLUs can be associated with different MIS. The stratigraphy and the thickness, and therefore the depth, of the RLUs are approximated.

Fig. 3. A) Hillshade map of the Digital Elevation Model (~2 m in resolution) based on Pleiades satellite imagery and the point of view for the stacked swath profiles. The white spots inside the hillshade correspond to the clouds in the

Pleiades images. **B)** Stacked swath profiles (600 profiles evenly distributed over the area shown in A, vertical exaggeration x6) and inner edges of the main CRTs at Cape Laundi (elevations are given in relation to the mean sea level). Most main CRTs show lateral morphological variability in the number of intermediate terraces, while the elevation of their inner edge is less varied, highlighting a uniform uplift rate along the coast.

Fig. 4. Sea level (SL) curves used in this study from **A)** 435 ka and **B)** 150 ka to today. MIS nomenclature (numbers and letters) from Railsback et al. (2015). SL highstands/lowstands of the different curves are generally coeval; however, they differ in their frequencies and amplitudes. For example, SL curves are at low (Waelbroeck et al., 2002; Bintanja et al., 2005), intermediate (Grant et al., 2014; Spratt and Lisiecki 2016), and high (Rohling et al., 2009) frequencies. SL rate peaks of the different curves are generally coeval; however, they differ in their frequencies and amplitudes. SL curves can show an episode of almost constant SL rise (Waelbroeck et al., 2002; Bintanja et al., 2005; Spratt and Lisiecki, 2016) or two episodes of SL change during the transgression before MIS 5e highstand (Rohling et al., 2009; Grant et al., 2014), and one (Waelbroeck et al., 2002; Bintanja et al., 2005; Grant et al., 2014; Spratt and Lisiecki, 2016) or several highstand peaks (Rohling et al., 2009).

Fig. 5. A) Morphometric profiles (dGPS and sonar) at Cape Laundi, showing the location and ages of U/Th and Electron spin resonance (ESR) samples (Pirazzoli et al., 1991, 1993; Bard et al., 1996). The small light brown box at top right corresponds to the dGPS 2 profile visible in Figs. 1 and 3. The most robust dating

correspond to those selected in section 3.4.. **B)** Best-fit numerical simulation (obtained with B05; U (uplift rate): 0.50 mm a^{-1}; G_{max} (maximum reef growth rate): 6 mm a^{-1}; E (erosion rate): 60 mm^3 a^{-1}; ɑ (initial slope): 6 %). The elevations and locations of the field inner edges were determined from the breaks in slope visible on the dGPS profiles. For the modeled inner edges this was determined by the breaks in slope and their consistency with the chrono-stratigraphic succession of the actual sequence. The red and green lines (near the y-axis) show the modeled elevations of the CRT inner edges, close to or different from field measurements, respectively. Two inner edges measured in the field (i.e., associated with CRT II_4, and II_0) do not correlate with any of the simulated inner edges (they are marked with a "?"). Conversely, one simulated inner edge (in the middle of simulated CRT I_1) does not correlate with any field measurements (also marked with a "?"). The full description of the simulated CRT sequence is in section 4.1..

Fig. 6. Parametric study, simulations scores for 5 eustatic sea level (ESL) curves (columns), uplift rates (U; rows), maximum reef growth rates (G_{max}; x axis) and erosion rates (E; y axis). The color of each “small box” represents the score of the simulation for a given parametrization based on the chrono-morphological criteria defined in section 3.3. Each “medium box” shows simulation scores for the range of maximum reef growth rate, G_{max}, and the range of erosional potential E (see section 3.3.). Each column of “medium boxes” shows the variability along the range of uplift rates. Each line of “medium boxes” shows the variability among ESL reconstructions. The best-fitting initial slope (ɑ) is indicated for each SL reconstruction. The best-fit simulations are surrounded by

a red square with the names designated in section 3.3. (i.e., W02, B05, R09, G14, and S16).

Fig. 7. Linear regression between field and simulated measurements for **A)** the elevation of the inner edges of CRTs and **B)** CRTs widths.

Fig. 8. Model predictions at present-day for various parametrizations (U: Uplift rate; G_{max}: maximum reef growth rate; E: erosion rate; α: Initial slope) and derived from the eustatic sea level curves of, **A)** Waelbroeck et al. (2002) (U: 0.45 mm a^{-1}; G_{max}: 6 mm a^{-1}; E: 60 mm^3 a^{-1}; α: 6 %), **B)** Rohling et al. (2009) (U: 0.46 mm a^{-1}; G_{max}: 6 mm a^{-1}; E: 60 mm^3 a^{-1}; α: 6 %) **C)** Grant et al. (2014) (U: 0.50 mm a^{-1}; G_{max}: 6 mm a^{-1}; E: 60 mm^3 a^{-1}; α: 7 %), and **D)** Spratt and Lisiecki (2016) (U: 0.45 mm a^{-1}; G_{max}: 6 mm a^{-1}; E: 60 mm^3 a^{-1}; α: 6 %).

Fig. 9. Formation of coral reef terraces (CTRs; same simulation as in Fig. 5B (B05)), at different time steps: **A)** 135, **B)** 130, **C)** 125, **D)** 120, **E)** 115, **F)** 113, **G)** 97, and **H)** 80 ka ago. These time steps are placed by stars on the sea level curve (from Bintanja et al., 2005) at the bottom left. At the bottom right is the color scale of the CRTs associated with the Marine Isotopic Stage. The description of CRTs morphogenesis can be found in sections 5.1. and 5.2..

Table captions

Table 1. Nomenclature (from Pirazzoli et al., 1991, 1993, and revised in this study), associated MIS (i.e., Marine Isotopic Stage), elevation, width of CRTs

from previous studies (Pirazzoli et al., 1991, 1993), dGPS (i.e., differential Global Positioning System) field measurements. The uncertainties of the elevation of former reef crests are those given by Pirazzoli et al (1991, 1993). Those of the inner edges correspond to the roughness of the terraces (as in Chauveau et al., 2021b).

Table 2. Most robust dating selected for Cap Laundi. All the information in this table come from Bard et al (1996). Elevations are relative to the present mean low water spring level and have been rounded to the nearest meters.

Table 3. Nomenclature (from this study), associated MIS inferred from B05, elevation, width of CRTs from dGPS field measurements and the best-fit simulation (i.e., B05). For best-fit simulation columns, ± 1 m corresponds to the spatial resolution of the model. For CRT widths, ± 1 m corresponds to the resolution of the Pleiades images (from which the DEM is derived), as these measurements were double-checked with these satellite images and the dGPS profile.

Supplementary Figure captions

Supplementary Information - W02-U0.45-Gmax06-E60-P06

A) Morphometric profiles (dGPS and sonar) at Cape Laundi, showing the location and ages of U/Th and Electron spin resonance (ESR) samples (Pirazzoli et al., 1991, 1993; Bard et al., 1996). **B)** Best-fit numerical simulation from the sea level reconstruction of Waelbroeck et al., (2002), i.e., W02; U (uplift rate): 0.45 mm a^{-1}; G_{max} (maximum reef growth rate): 6 mm a^{-1}; E (erosion rate): 60 mm^3 a^{-1}; ɑ (initial slope): 6 %)). The red and green lines (near the y-axis) show the modeled elevations of the coral reef terrace (CRT) inner edges, close to or different from field measurements, respectively.

Supplementary Information - R09-U0.46-Gmax06-E60-P06

A) Morphometric profiles (dGPS and sonar) at Cape Laundi, showing the location and ages of U/Th and Electron spin resonance (ESR) samples (Pirazzoli et al., 1991, 1993; Bard et al., 1996). **B)** Best-fit numerical simulation from the sea level reconstruction of Rohling et al., (2009), i.e., R09; U (uplift rate): 0.46 mm a^{-1}; G_{max} (maximum reef growth rate): 6 mm a^{-1}; E (erosion rate): 60 mm^3 a^{-1}; ɑ (initial slope): 6 %)). The red and green lines (near the y-axis) show the modeled elevations of the coral reef terrace (CRT) inner edges, close to or different from field measurements, respectively.

Supplementary Information - G14-U0.50-Gmax06-E60-P07

A) Morphometric profiles (dGPS and sonar) at Cape Laundi, showing the location and ages of U/Th and Electron spin resonance (ESR) samples (Pirazzoli et al., 1991, 1993; Bard et al., 1996). **B)** Best-fit numerical simulation from the sea level reconstruction of Grant et al., (2014), i.e., G14; U (uplift rate): 0.50 mm a^{-1}; G_{max} (maximum reef growth rate): 6 mm a^{-1}; E (erosion rate): 60 mm^3 a^{-1}; ɑ (initial slope): 7 %. The red and green lines (near the y-axis) show the modeled elevations of the coral reef terrace (CRT) inner edges, close to or different from field measurements, respectively.

Supplementary Information - S16-U0.45-Gmax06-E60-P06

A) Morphometric profiles (dGPS and sonar) at Cape Laundi, showing the location and ages of U/Th and Electron spin resonance (ESR) samples (Pirazzoli et al., 1991, 1993; Bard et al., 1996). **B)** Best-fit numerical simulation from the sea level reconstruction of Spratt and Lisiecki (2016), i.e., S16; U (uplift rate): 0.45 mm a^{-1}; G_{max} (maximum reef growth rate): 6 mm a^{-1}; E (erosion rate): 60 mm^3 a^{-1}; ɑ (initial slope): 6 %. The red and green lines (near the y-axis) show the modeled elevations of the coral reef terrace (CRT) inner edges, close to or different from field measurements, respectively.

Supplementary Information – B05-U0.2-Gmax06-E60-P06

Morphometric profiles (dGPS and sonar) at Cape Laundi, showing the location and ages of U/Th and Electron spin resonance (ESR) samples (Pirazzoli et al., 1991, 1993; Bard et al., 1996) and numerical simulation from the sea level reconstruction of Bintanja et al., (2005), i.e., B05; U (uplift rate): 0.20 mm a^{-1}; G_{max} (maximum reef growth rate): 6 mm a^{-1}; E (erosion rate): 60 mm^3 a^{-1}; α (initial slope): 6 %.

Supplementary Information – W02-U0.68-Gmax08-E60-P06

Morphometric profiles (dGPS and sonar) at Cape Laundi, showing the location and ages of U/Th and Electron spin resonance (ESR) samples (Pirazzoli et al., 1991, 1993; Bard et al., 1996) and numerical simulation from the sea level reconstruction of Waelbroeck., (2002), i.e., W02; U (uplift rate): 0.68 mm a^{-1}; G_{max} (maximum reef growth rate): 8 mm a^{-1}; E (erosion rate): 60 mm^3 a^{-1}; α (initial slope): 6 %.

Supplementary Information – B05-U0.50-Gmax06-E20-P06

Morphometric profiles (dGPS and sonar) at Cape Laundi, showing the location and ages of U/Th and Electron spin resonance (ESR) samples (Pirazzoli et al., 1991, 1993; Bard et al., 1996) and numerical simulation from the sea level reconstruction of Bintanja et al., (2005), i.e., B05; U (uplift rate): 0.50 mm a^{-1}; G_{max} (maximum reef growth rate): 6 mm a^{-1}; E (erosion rate): 20 mm^3 a^{-1}; α (initial slope): 6 %.

Supplementary Information – B05-U0.50-Gmax14-E60-P06

Morphometric profiles (dGPS and sonar) at Cape Laundi, showing the location and ages of U/Th and Electron spin resonance (ESR) samples (Pirazzoli et al., 1991, 1993; Bard et al., 1996) and numerical simulation from the sea level reconstruction of Bintanja et al., (2005), i.e., B05; U (uplift rate): 0.50 mm a^{-1}; G_{max} (maximum reef growth rate): 14 mm a^{-1}; E (erosion rate): 60 mm^3 a^{-1}; α (initial slope): 6 %.

Supplementary Animation captions

Supplementary Information – S1 - B05 animation

This animation is realised over the past 800 ka with the best-fit numerical simulation from the sea level reconstruction of Bintanja et al., (2005), i.e., B05, and with U (uplift rate): 0.50 mm a^{-1}, G_{max} (maximum reef growth rate): 6 mm a^{-1}, E (erosion rate): 60 mm^3 a^{-1}, and α (initial slope): 6 %.

Supplementary Information – S2 - W02 animation

This animation is realised over the past 800 ka with the best-fit numerical simulation from the sea level reconstruction of Waelbroeck et al., (2002), i.e., W02, and with U (uplift rate): 0.45 mm a^{-1}, G_{max} (maximum reef growth rate): 6 mm a^{-1}, E (erosion rate): 60 mm^3 a^{-1}, and α (initial slope): 6 %. From 800 ka to 430 ka, the sea level reconstruction of Bintanja et al, (2005) is used, from 430 ka to 0 ka the sea level reconstruction of Waelbroeck et al., (2002).

Supplementary Information – S3 - R09 animation

This animation is realised over the past 800 ka with the best-fit numerical simulation from the sea level reconstruction of Rohling et al., (2009), i.e., R09, and with U (uplift rate): 0.46 mm a^{-1}, G_{max} (maximum reef growth rate): 6 mm a^{-1}, E (erosion rate): 60 mm^3 a^{-1}, and α (initial slope): 6 %. From 800 ka to 430 ka, the sea level reconstruction of Bintanja et al, (2005) is used, from 500 ka to 0 ka the sea level reconstruction of Rohling et al., (2009).

Supplementary Information – S4 - G14 animation

This animation is realised over the past 800 ka with the best-fit numerical simulation from the sea level reconstruction of Grant et al., (2014), i.e., G14, and with U (uplift rate): 0.50 mm a^{-1}, G_{max} (maximum reef growth rate): 6 mm a^{-1}, E (erosion rate): 60 mm^3 a^{-1}, and ɑ (initial slope): 7 %. From 800 ka to 430 ka, the sea level reconstruction of Bintanja et al, (2005) is used, from 500 ka to 0 ka the sea level reconstruction of Grant et al., (2014).

Supplementary Information – S5 - S16 animation

This animation is realised over the past 800 ka with the best-fit numerical simulation from the sea level reconstruction of Spratt and Lisiecki, i.e., S16, and with U (uplift rate): 0.45 mm a^{-1}, G_{max} (maximum reef growth rate): 6 mm a^{-1}, E (erosion rate): 60 mm^3 a^{-1}, and ɑ (initial slope): 6 %.

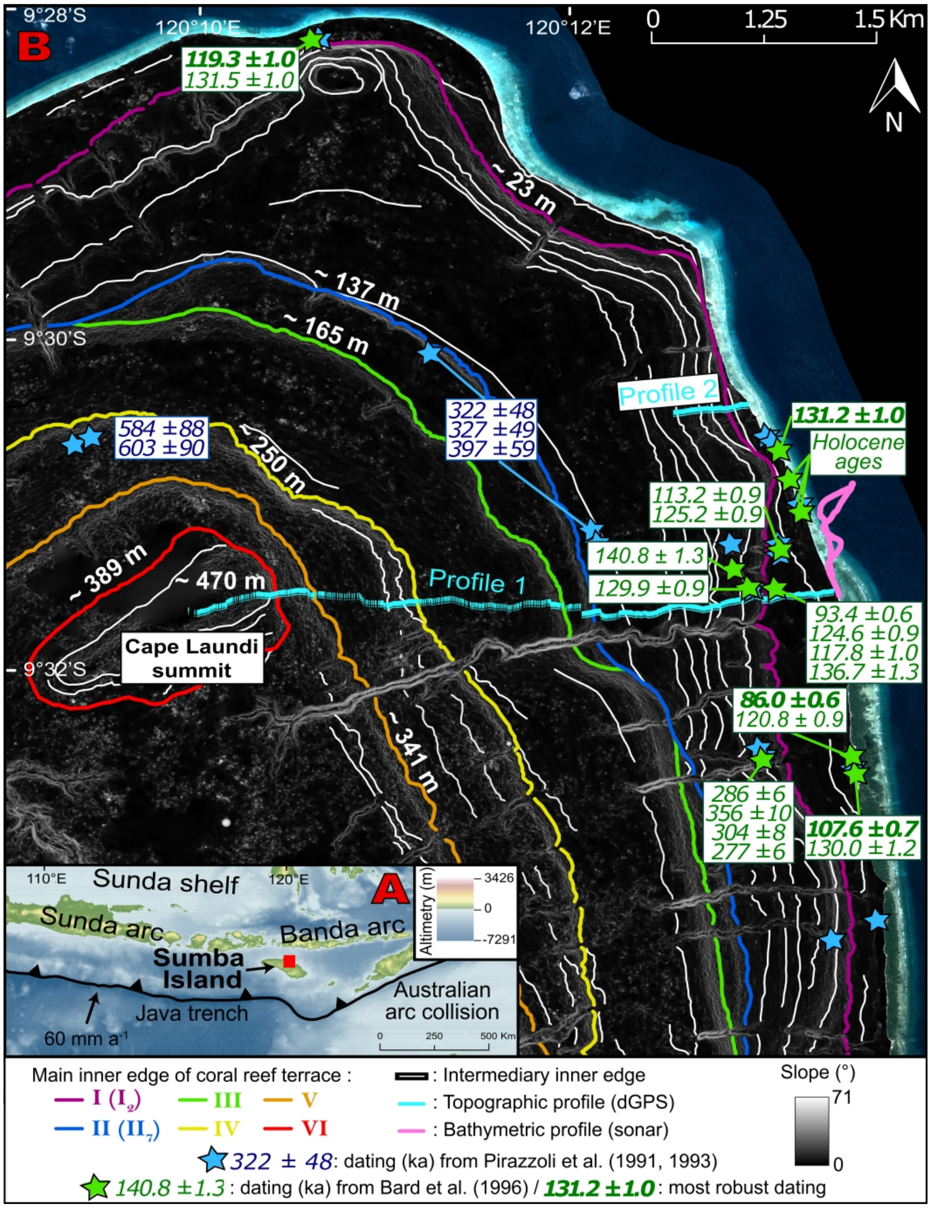

Fig. 1. A) Altimetry map of Southeast Indonesia and location of Sumba Island and Cape Laundi (red square). Elevation data from the Shuttle Radar Topography Mission (SRTM), and bathymetry data from the General Bathymetric Chart of Oceans (GEBCO), both at 90 m resolution. B) Slope map of Cape Laundi from Pleiades satellite imagery. Contours delineate the inner edges of the CRTs, and we indicate the location of previously dated samples (U/Th and Electron Spin Resonance dating; Pirazzoli et al., 1991, 1993; Bard et al., 1996). The most robust dating correspond to those selected in section 3.4.. Several dates are sometimes present in a single box because the dating samples were very close to each other (see Fig. 1 in Bard et al., 1996 and Fig. 2 in Pirazzoli et al., 1993). Some blue stars have no associated dating because this is not specified in the study of Pirazzoli et al. (1993). The light blue dotted line and the pink line indicate topographic (dGPS) and bathymetric (sonar) profile, respectively.

1016x1317mm (120 x 120 DPI)

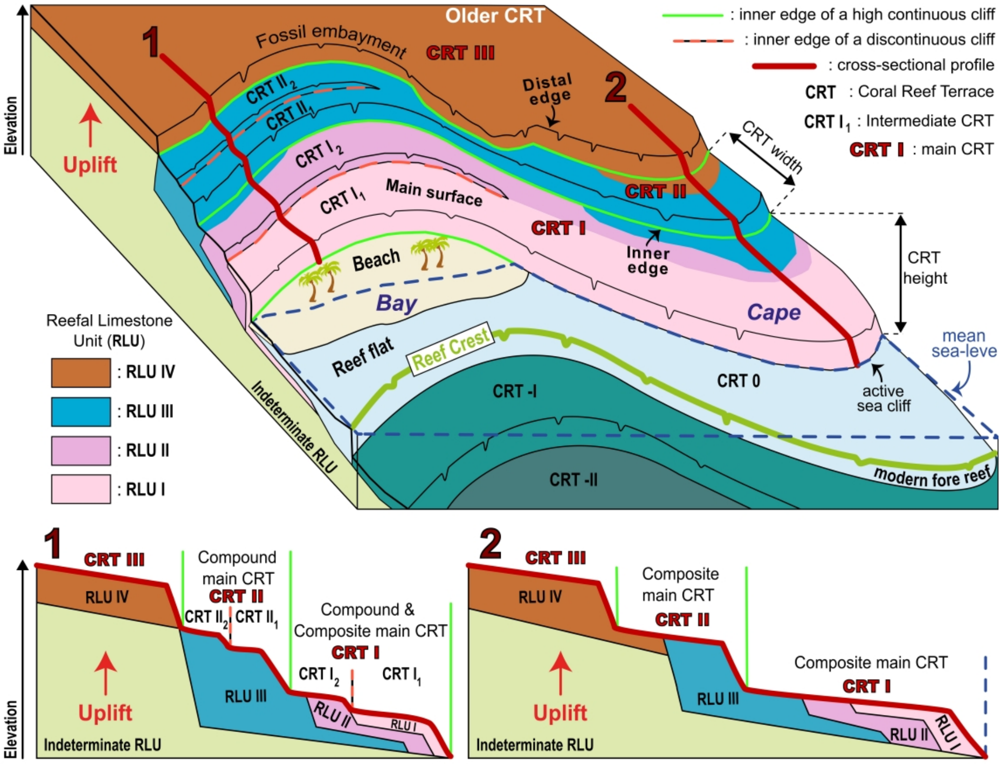

Fig. 2. Sketch of a sequence of coral reef terraces (CRTs), modified from Pedoja et al. (2018), highlighting a high variability of sequence morphology that can occur for a uniform uplift. The inner edges of the main CRT I and CRT II are continuous from the bay to the cape, the inner edges of the CRT I1 and CRT II1 are not. Depending on the location along the coast (Bay or Cape), the main CRT II is either compound, i.e., consisting of two CRTs (i.e., CRT II1 et II2) but a single reefal limestone unit (i.e., RLU III; Profile 1), or composite, i.e., consisting of a single CRT (i.e., CRT II) but including several RLUs (i.e., RLU III and IV; Profile 2). The RLUs can be associated with different MIS. The stratigraphy and the thickness, and therefore the depth, of the RLUs are approximated.

1028x784mm (120 x 120 DPI)

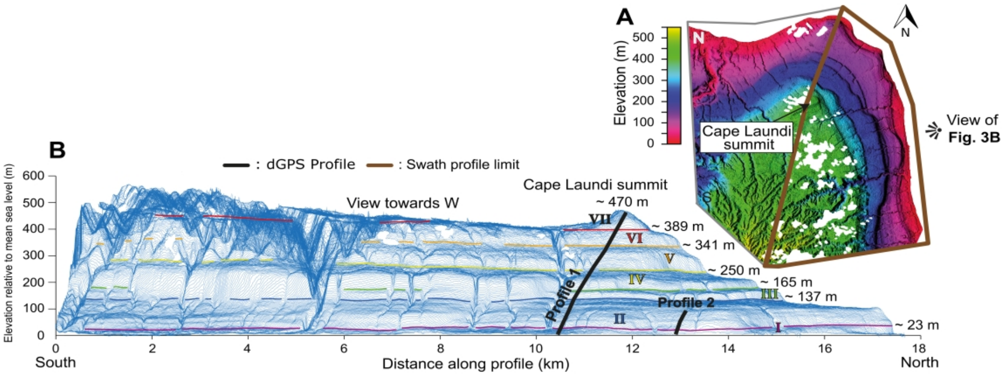

Fig. 3. A) Hillshade map of the Digital Elevation Model (~2 m in resolution) based on Pleiades satellite imagery and the point of view for the stacked swath profiles. The white spots inside the hillshade correspond to the clouds in the Pleiades images. B) Stacked swath profiles (600 profiles evenly distributed over the area shown in A, vertical exaggeration x6) and inner edges of the main CRTs at Cape Laundi (elevations are given in relation to the mean sea level). Most main CRTs show lateral morphological variability in the number of intermediate terraces, while the elevation of their inner edge is less varied, highlighting a uniform uplift rate along the coast.

1460x541mm (120 x 120 DPI)

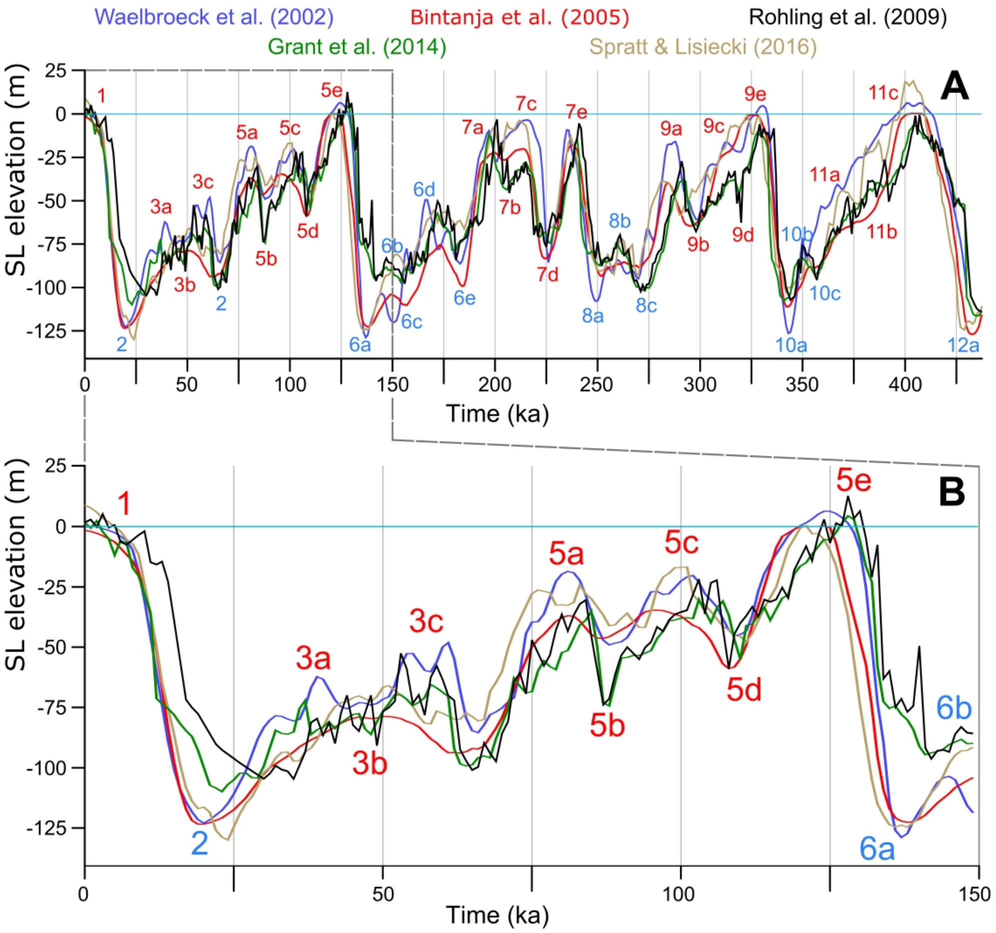

Fig. 4. Sea level (SL) curves used in this study from A) 435 ka and B) 150 ka to today. MIS nomenclature (numbers and letters) from Railsback et al. (2015). SL highstands/lowstands of the different curves are generally coeval; however, they differ in their frequencies and amplitudes. For example, SL curves are at low (Waelbroeck et al., 2002; Bintanja et al., 2005), intermediate (Grant et al., 2014; Spratt and Lisiecki 2016), and high (Rohling et al., 2009) frequencies. SL rate peaks of the different curves are generally coeval; however, they differ in their frequencies and amplitudes. SL curves can show an episode of almost constant SL rise (Waelbroeck et al., 2002; Bintanja et al., 2005; Spratt and Lisiecki, 2016) or two episodes of SL change during the transgression before MIS 5e highstand (Rohling et al., 2009; Grant et al., 2014), and one (Waelbroeck et al., 2002; Bintanja et al., 2005; Grant et al., 2014; Spratt and Lisiecki, 2016) or several highstand peaks (Rohling et al., 2009).

1390x1302mm (120 x 120 DPI)

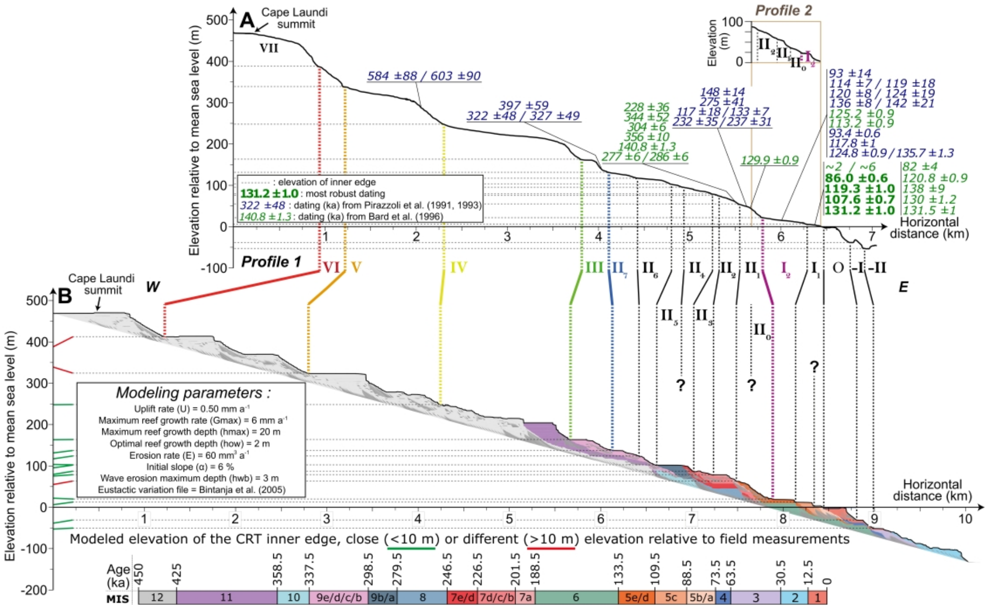

Fig. 5. A) Morphometric profiles (dGPS and sonar) at Cape Laundi, showing the location and ages of U/Th and Electron spin resonance (ESR) samples (Pirazzoli et al., 1991, 1993; Bard et al., 1996). The small light brown box at top right corresponds to the dGPS 2 profile visible in Figs. 1 and 3. The most robust dating correspond to those selected in section 3.4.. B) Best-fit numerical simulation (obtained with B05; U (uplift rate): 0.50 mm a-1; Gmax (maximum reef growth rate): 6 mm a-1; E (erosion rate): 60 mm3 a-1; α (initial slope): 6 %). The elevations and locations of the field inner edges were determined from the breaks in slope visible on the dGPS profiles. For the modeled inner edges this was determined by the breaks in slope and their consistency with the chrono-stratigraphic succession of the actual sequence. The red and green lines (near the y-axis) show the modeled elevations of the CRT inner edges, close to or different from field measurements, respectively. Two inner edges measured in the field (i.e., associated with CRT II4, and II0) do not correlate with any of the simulated inner edges (they are marked with a "?"). Conversely, one simulated inner edge (in the middle of simulated CRT I1) does not correlate with any field measurements (also marked with a "?"). The full description of the simulated CRT sequence is in section 4.1..

1352x837mm (120 x 120 DPI)

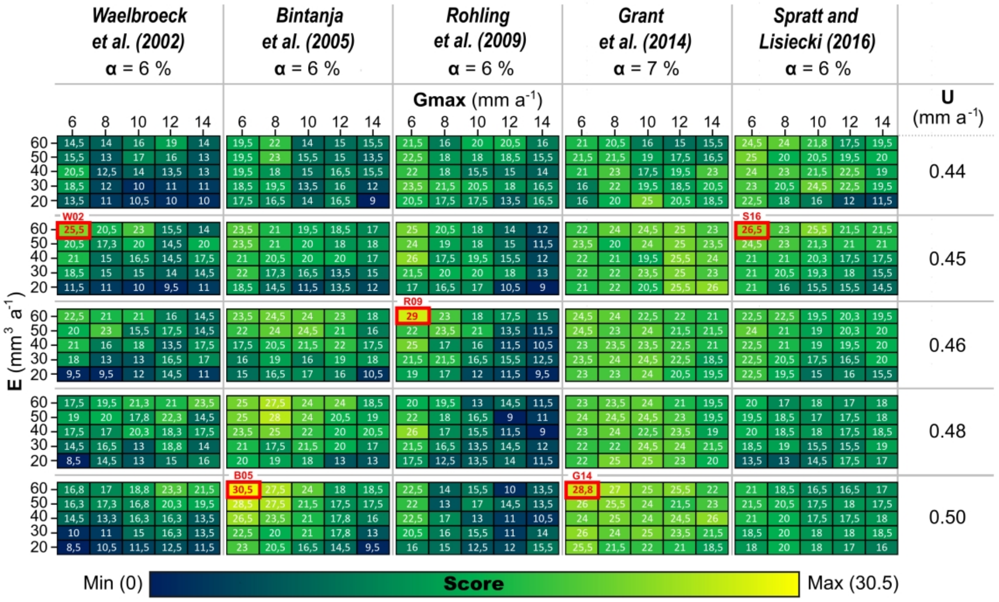

U (mm a^{-1})	E (mm^3 a^{-1})	*Waelbroeck et al. (2002)* α = 6 %					*Bintanja et al. (2005)* α = 6 %					*Rohling et al. (2009)* α = 6 %					*Grant et al. (2014)* α = 7 %					*Spratt and Lisiecki (2016)* α = 6 %				
	Gmax (mm a^{-1})	6	8	10	12	14	6	8	10	12	14	6	8	10	12	14	6	8	10	12	14	6	8	10	12	14
0.44	60	14,5	14	16	19	14	19,5	22	14	15	15,5	21,5	16	20	20,5	16	21	20,5	16	15	15,5	24,5	24	21,8	17,5	19,5
	50	15,5	13	17	16	13	19,5	23	15,5	15	13,5	22,5	18	18	18,5	15,5	21,5	21,5	19	17,5	16,5	25	20	20,5	19,5	20
	40	20,5	12,5	14	13,5	13	19,5	18	15	16,5	15,5	22	18	15,5	15	14	21	23	17,5	19,5	23	24	23	21,5	22,5	19
	30	18,5	12	10	11	11	18,5	19,5	13,5	16	12	23,5	21,5	20,5	18	16,5	16	22	19,5	18,5	20,5	23	20,5	24,5	22,5	19,5
	20	13,5	11	10,5	10	10	17,5	16,5	14	16,5	9	20,5	17,5	17,5	13,5	16,5	16	20	25	20,5	18,5	22,5	18	16	12	11,5
0.45	60	25,5	20,5	23	15,5	14	23,5	21	19,5	18,5	17	25	20,5	18	14	12	22	24	24,5	25	23	26,5	23	25,5	21,5	21,5
	50	20,5	17,3	20	14,5	20	23,5	21	20	18	18	24	19	18	15	11,5	23,5	20	24	25	23,5	24,5	23	21,3	21	21
	40	21	15	16,5	14,5	17,5	21	20,5	20	20	17	26	17,5	19,5	15,5	12	22	21	19,5	25,5	24	21	21	20,3	17,5	17,5
	30	18,5	15	15	14	14,5	22	17,3	16,5	13,5	15	21,5	20	20	18	13	22	22	23,5	25	23	21	20,5	19,3	18	15,5
	20	11,5	11	10	9,5	11	18,5	14,5	11,5	13,5	12	17	16,5	17	10,5	9	21	22	20,5	25,5	26	21	16	15,5	15,5	14,5
0.46	60	22,5	21	21	16	14,5	23,5	24,5	24	23	18	29	23	18	17,5	15	24,5	24	22,5	22	21	22,5	22,5	19,5	20,3	19,5
	50	20	23	15,5	17,5	14,5	22	24	24,5	21	16	22	23,5	21	13,5	11,5	24,5	23	24	21,5	21,5	24	21	19	20,3	20
	40	21	16	18	13,5	17,5	17,5	20,5	21,5	22	17,5	25	17	16	11,5	10,5	23	23,5	23,5	22,5	21	22,5	21	19	19,5	20
	30	18	13	13	16,5	17	16	19	16	19	18	21,5	21,5	16,5	15,5	12,5	23,5	24	24,5	22,5	18,5	22,5	20,5	17,5	16,5	20
	20	9,5	9,5	12	14,5	11	15	16,5	17	16	10,5	19	17	12	11,5	9,5	23	23	24	20,5	19,5	22,5	19,5	15	16	15,5
0.48	60	17,5	19,5	21,3	21	23,5	25	27,5	24	24	18,5	20	19,5	13	14,5	11,5	23	23,5	24	21	19,5	20	17	18	17	18
	50	19	20	17,8	22,3	14,5	25	28	24	20,5	19	22	18	16,5	9	11	24	24,5	24,5	23	19,5	19,5	18,5	17	17,5	18
	40	17,5	17	20,3	18,3	17,5	23,5	25	22	20	20,5	26	17	15,5	11,5	9	23	24	22,5	23,5	19	20	18,5	18	17,5	18,5
	30	14,5	16,5	13	18,8	14	21	17,5	21,5	20	17	21,5	16,5	13,5	14,5	12	22	22	24,5	24	21,5	18,5	19	15,5	15,5	19
	20	8,5	14,5	13	15	16	20	19	18	13	13	17,5	12,5	13,5	14	11,5	22	25	25	23	20	13,5	13	14,5	17,5	17
0.50	60	16,8	17	18,8	23,3	21,5	30,5	27,5	24	18	18,5	22,5	14	15,5	10	13,5	28,8	27	25	25,5	22	21	18,5	16,5	16,5	17
	50	16,3	17,3	16,8	20,3	19,5	28,5	27,5	21,5	17,5	17,5	22	13	17	14,5	13,5	26	25,5	24	21,5	23	21,5	20,5	17,5	18	17,5
	40	14,5	13,3	16,3	16,3	13,5	26,5	23,5	21	17,8	16	22,5	17	13	11	10,5	24	25	24	24,5	26	21	20	17,5	17,5	18
	30	10	11	15	16,3	13,5	22,5	20	21	17,8	13	20,5	16	15,5	11	14	26	24	25	23,5	21,5	18,5	20	18	18	18,5
	20	8,5	10,5	11,5	12,5	11,5	23	20,5	16,5	14,5	9,5	16	15	12,5	12	15,5	25,5	21,5	22	21	18,5	18	20	18	17	16

Fig. 6. Parametric study, simulations scores for 5 eustatic sea level (ESL) curves (columns), uplift rates (U; rows), maximum reef growth rates (Gmax; x axis) and erosion rates (E; y axis). The color of each "small box" represents the score of the simulation for a given parametrization based on the chrono-morphological criteria defined in section 3.3. Each "medium box" shows simulation scores for the range of maximum reef growth rate, Gmax, and the range of erosional potential E (see section 3.3.). Each column of "medium boxes" shows the variability along the range of uplift rates. Each line of "medium boxes" shows the variability among ESL reconstructions. The best-fitting initial slope (α) is indicated for each SL reconstruction. The best-fit simulations are surrounded by a red square with the names designated in section 3.3. (i.e., W02, B05, R09, G14, and S16).

845x513mm (120 x 120 DPI)

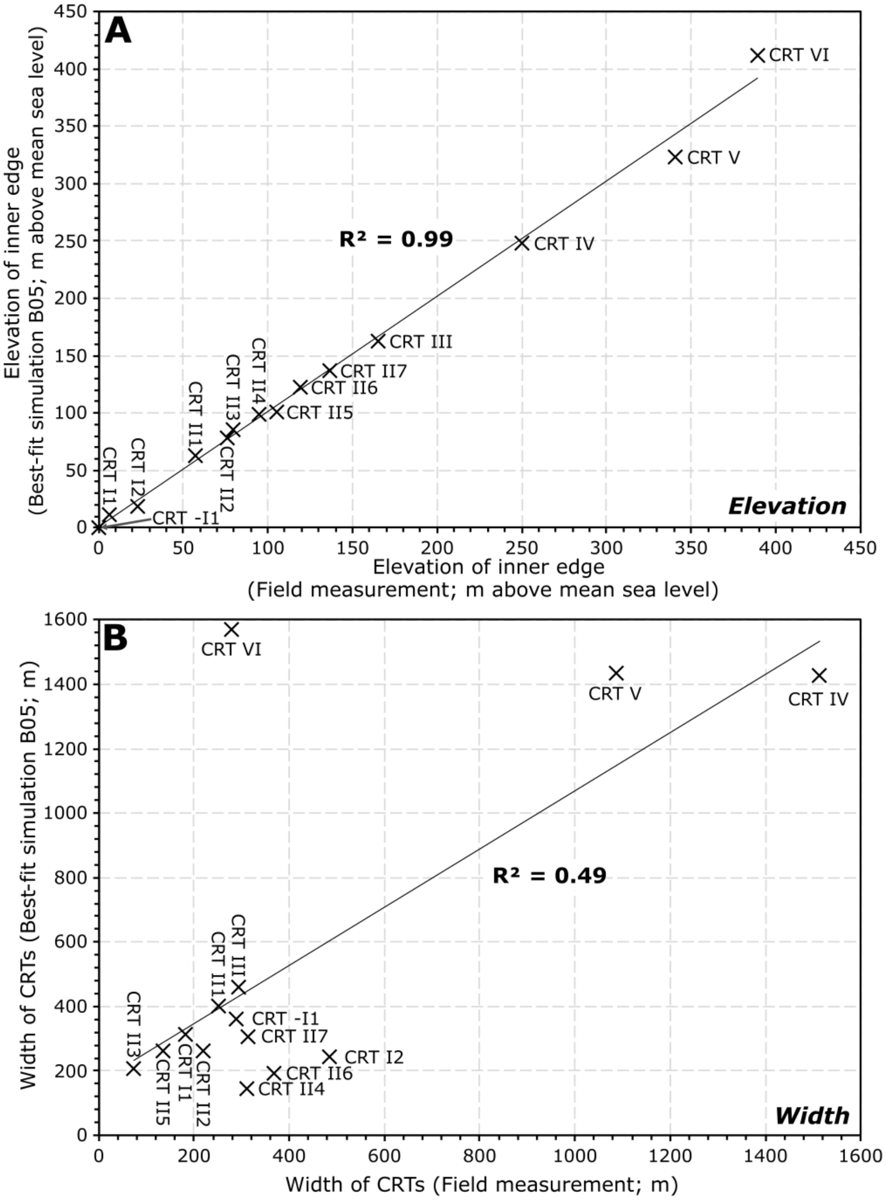

Fig. 7. Linear regression between field and simulated measurements for A) the elevation of the inner edges of CRTs and B) CRTs widths.

963x1292mm (120 x 120 DPI)

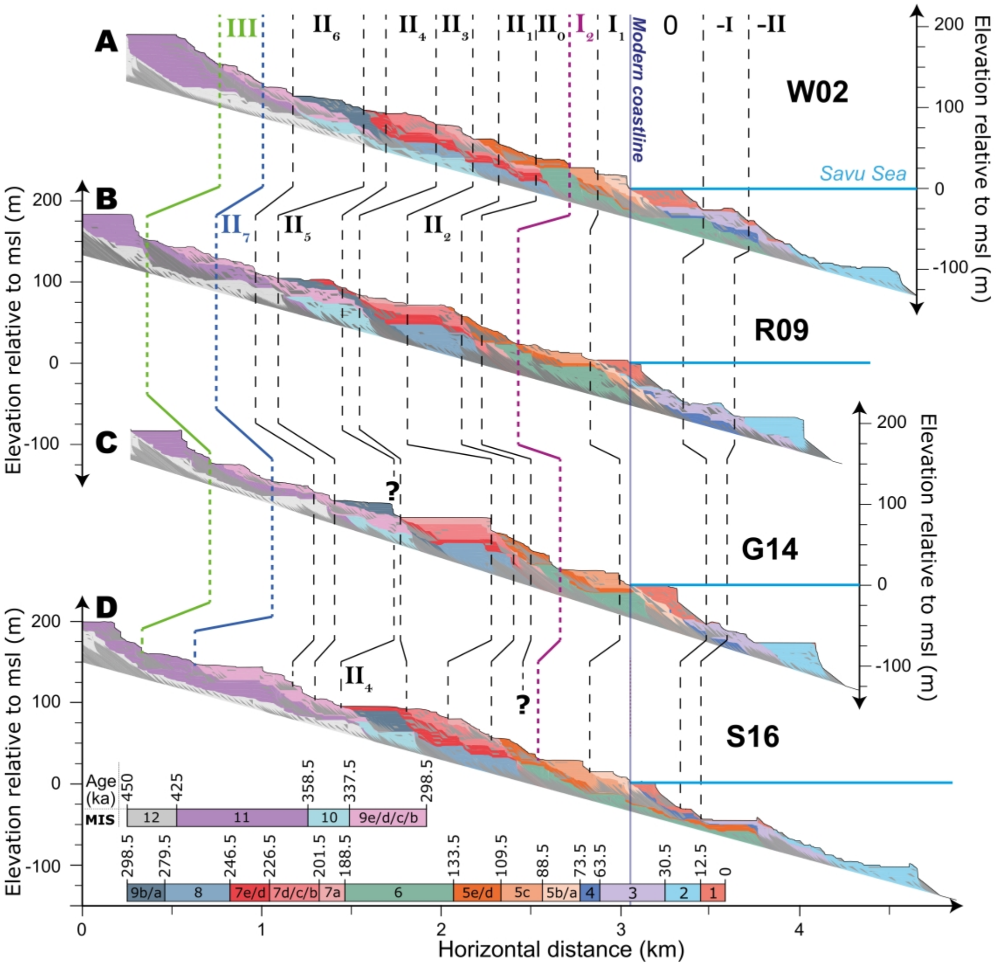

Fig. 8. Model predictions at present-day for various parametrizations (U: Uplift rate; Gmax: maximum reef growth rate; E: erosion rate; α: Initial slope) and derived from the eustatic sea level curves of, A) Waelbroeck et al. (2002) (U: 0.45 mm a-1; Gmax: 6 mm a-1; E: 60 mm3 a-1; α: 6 %), B) Rohling et al. (2009) (U: 0.46 mm a-1; Gmax: 6 mm a-1; E: 60 mm3 a-1; α: 6 %) C) Grant et al. (2014) (U: 0.50 mm a-1; Gmax: 6 mm a-1; E: 60 mm3 a-1; α: 7 %), and D) Spratt and Lisiecki (2016) (U: 0.45 mm a-1; Gmax: 6 mm a-1; E: 60 mm3 a-1; α: 6 %).

1033x1000mm (120 x 120 DPI)

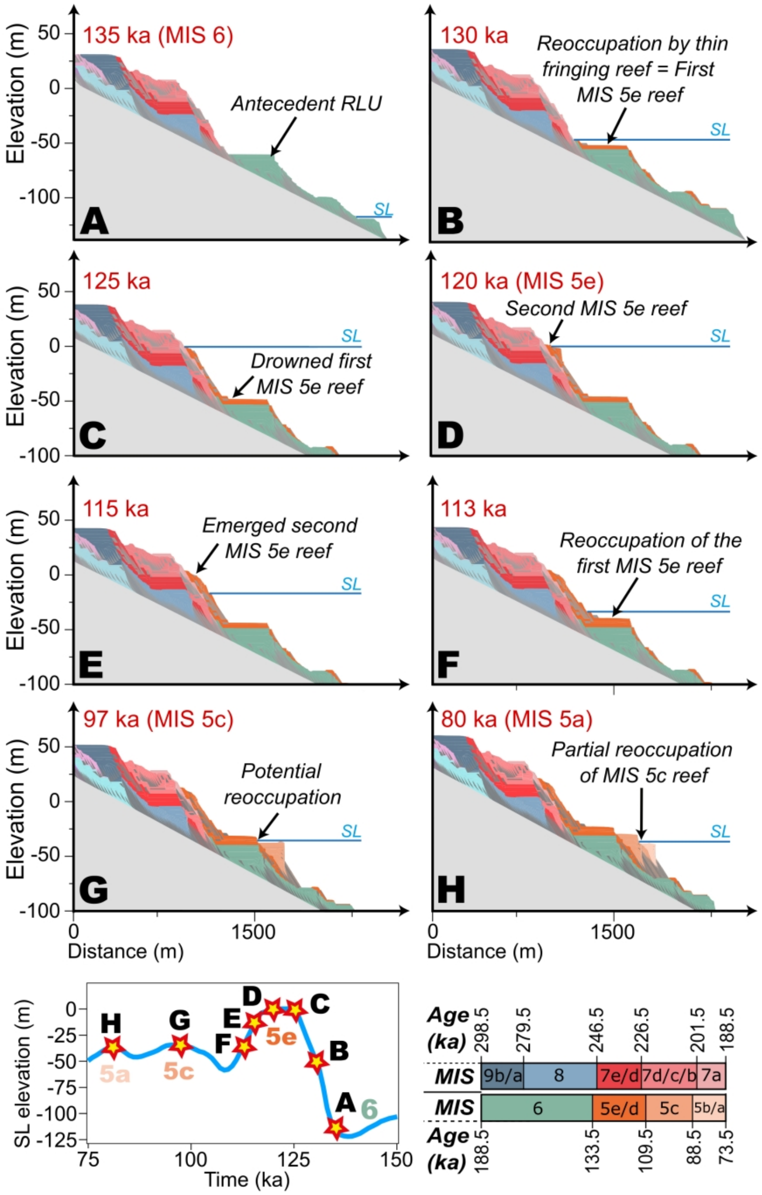

Fig. 9. Formation of coral reef terraces (CRTs; same simulation as in Fig. 5B (B05)), at different time steps: A) 135, B) 130, C) 125, D) 120, E) 115, F) 113, G) 97, and H) 80 ka ago. These time steps are placed by stars on the sea level curve (from Bintanja et al., 2005) at the bottom left. At the bottom right is the color scale of the CRTs associated with the Marine Isotopic Stage. The description of CRTs morphogenesis can be found in sections 5.1. and 5.2..

397x616mm (120 x 120 DPI)

Supporting information captions

Supporting Information - W02-U0.45-Gmax06-E60-P06

A) Morphometric profiles (dGPS and sonar) at Cape Laundi, showing the location and ages of U/Th and Electron spin resonance (ESR) samples (Pirazzoli et al., 1991, 1993; Bard et al., 1996). **B)** Best-fit numerical simulation from the sea level reconstruction of Waelbroeck et al., (2002), i.e., W02; U (uplift rate): 0.45 mm a^{-1}; G_{max} (maximum reef growth rate): 6 mm a^{-1}; E (erosion rate): 60 mm^3 a^{-1}; ɑ (initial slope): 6 %)). The red and green lines (near the y-axis) show the modeled elevations of the coral reef terrace (CRT) inner edges, close to or different from field measurements, respectively.

Supporting Information - R09-U0.46-Gmax06-E60-P06

A) Morphometric profiles (dGPS and sonar) at Cape Laundi, showing the location and ages of U/Th and Electron spin resonance (ESR) samples (Pirazzoli et al., 1991, 1993; Bard et al., 1996). **B)** Best-fit numerical simulation from the sea level reconstruction of Rohling et al., (2009), i.e., R09; U (uplift rate): 0.46 mm a^{-1}; G_{max} (maximum reef growth rate): 6 mm a^{-1}; E (erosion rate): 60 mm^3 a^{-1}; ɑ (initial slope): 6 %)). The red and green lines (near the y-axis) show the modeled elevations of the coral reef terrace (CRT) inner edges, close to or different from field measurements, respectively.

Supporting Information - G14-U0.50-Gmax06-E60-P07

A) Morphometric profiles (dGPS and sonar) at Cape Laundi, showing the location and ages of U/Th and Electron spin resonance (ESR) samples (Pirazzoli et al., 1991, 1993; Bard et al., 1996). **B)** Best-fit numerical simulation from the sea level reconstruction of Grant et al., (2014), i.e., G14; U (uplift rate): 0.50 mm a^{-1}; G_{max} (maximum reef growth rate): 6 mm a^{-1}; E (erosion rate): 60 mm^3 a^{-1}; ɑ (initial slope): 7 %. The red and green lines (near the y-axis) show the modeled elevations of the coral reef terrace (CRT) inner edges, close to or different from field measurements, respectively.

Supporting Information - S16-U0.45-Gmax06-E60-P06

A) Morphometric profiles (dGPS and sonar) at Cape Laundi, showing the location and ages of U/Th and Electron spin resonance (ESR) samples (Pirazzoli et al., 1991, 1993; Bard et al., 1996). **B)** Best-fit numerical simulation from the sea level reconstruction of Spratt and Lisiecki (2016), i.e., S16; U (uplift rate): 0.45 mm a^{-1}; G_{max} (maximum reef growth rate): 6 mm a^{-1}; E (erosion rate): 60 mm^3 a^{-1}; ɑ (initial slope): 6 %. The red and green lines (near the y-axis) show the modeled elevations of the coral reef terrace (CRT) inner edges, close to or different from field measurements, respectively.

Supporting Information – B05-U0.2-Gmax06-E60-P06

Morphometric profiles (dGPS and sonar) at Cape Laundi, showing the location and ages of U/Th and Electron spin resonance (ESR) samples (Pirazzoli et al., 1991, 1993; Bard et al., 1996) and numerical simulation from the sea level reconstruction of Bintanja et al., (2005), i.e., B05; U (uplift rate): 0.20 mm a^{-1}; G_{max} (maximum reef growth rate): 6 mm a^{-1}; E (erosion rate): 60 mm^3 a^{-1}; α (initial slope): 6 %.

Supporting Information – W02-U0.68-Gmax08-E60-P06

Morphometric profiles (dGPS and sonar) at Cape Laundi, showing the location and ages of U/Th and Electron spin resonance (ESR) samples (Pirazzoli et al., 1991, 1993; Bard et al., 1996) and numerical simulation from the sea level reconstruction of Waelbroeck., (2002), i.e., W02; U (uplift rate): 0.68 mm a^{-1}; G_{max} (maximum reef growth rate): 8 mm a^{-1}; E (erosion rate): 60 mm^3 a^{-1}; α (initial slope): 6 %.

Supporting Information – B05-U0.50-Gmax06-E20-P06

Morphometric profiles (dGPS and sonar) at Cape Laundi, showing the location and ages of U/Th and Electron spin resonance (ESR) samples (Pirazzoli et al., 1991, 1993; Bard et al., 1996) and numerical simulation from the sea level reconstruction of Bintanja et al., (2005), i.e., B05; U (uplift rate): 0.50 mm a^{-1}; G_{max} (maximum reef growth rate): 6 mm a^{-1}; E (erosion rate): 20 mm^3 a^{-1}; α (initial slope): 6 %.

Supporting Information – B05-U0.50-Gmax14-E60-P06

Morphometric profiles (dGPS and sonar) at Cape Laundi, showing the location and ages of U/Th and Electron spin resonance (ESR) samples (Pirazzoli et al., 1991, 1993; Bard et al., 1996) and numerical simulation from the sea level reconstruction of Bintanja et al., (2005), i.e., B05; U (uplift rate): 0.50 mm a^{-1}; G_{max} (maximum reef growth rate): 14 mm a^{-1}; E (erosion rate): 60 mm^3 a^{-1}; α (initial slope): 6 %.

Supporting information captions – Animation

Supporting Information – S1 - B05 animation

This animation is realised over the past 800 ka with the best-fit numerical simulation from the sea level reconstruction of Bintanja et al., (2005), i.e., B05, and with U (uplift rate): 0.50 mm a^{-1}, G_{max} (maximum reef growth rate): 6 mm a^{-1}, E (erosion rate): 60 mm^3 a^{-1}, and α (initial slope): 6 %.

Supporting Information – S2 - W02 animation

This animation is realised over the past 800 ka with the best-fit numerical simulation from the sea level reconstruction of Waelbroeck et al., (2002), i.e., W02, and with U (uplift rate): 0.45 mm a^{-1}, G_{max} (maximum reef growth rate): 6 mm a^{-1}, E (erosion rate): 60 mm^3 a^{-1}, and α (initial slope): 6 %. From 800 ka to 430 ka, the sea level reconstruction of Bintanja et al, (2005) is used, from 430 ka to 0 ka the sea level reconstruction of Waelbroeck et al., (2002).

Supporting Information – S3 - R09 animation

This animation is realised over the past 800 ka with the best-fit numerical simulation from the sea level reconstruction of Rohling et al., (2009), i.e., R09, and with U (uplift rate): 0.46 mm a^{-1}, G_{max} (maximum reef growth rate): 6 mm a^{-1}, E (erosion rate): 60 mm^3 a^{-1}, and ɑ (initial slope): 6 %. From 800 ka to 430 ka, the sea level reconstruction of Bintanja et al, (2005) is used, from 500 ka to 0 ka the sea level reconstruction of Rohling et al., (2009).

Supporting Information – S4 - G14 animation

This animation is realised over the past 800 ka with the best-fit numerical simulation from the sea level reconstruction of Grant et al., (2014), i.e., G14, and with U (uplift rate): 0.50 mm a^{-1}, G_{max} (maximum reef growth rate): 6 mm a^{-1}, E (erosion rate): 60 mm^3 a^{-1}, and ɑ (initial slope): 7 %. From 800 ka to 430 ka, the sea level reconstruction of Bintanja et al, (2005) is used, from 500 ka to 0 ka the sea level reconstruction of Grant et al., (2014).

Supporting Information – S5 - S16 animation

This animation is realised over the past 800 ka with the best-fit numerical simulation from the sea level reconstruction of Spratt and Lisiecki, i.e., S16, and with U (uplift rate): 0.45 mm a^{-1}, G_{max} (maximum reef growth rate): 6 mm a^{-1}, E (erosion rate): 60 mm^3 a^{-1}, and ɑ (initial slope): 6 %.

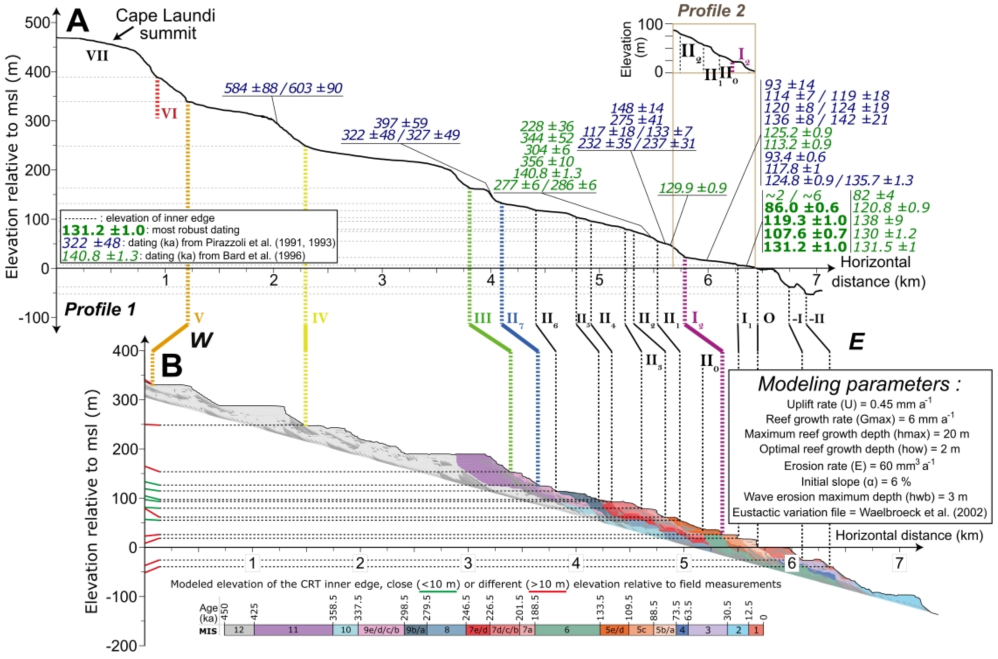

900x596mm (120 x 120 DPI)

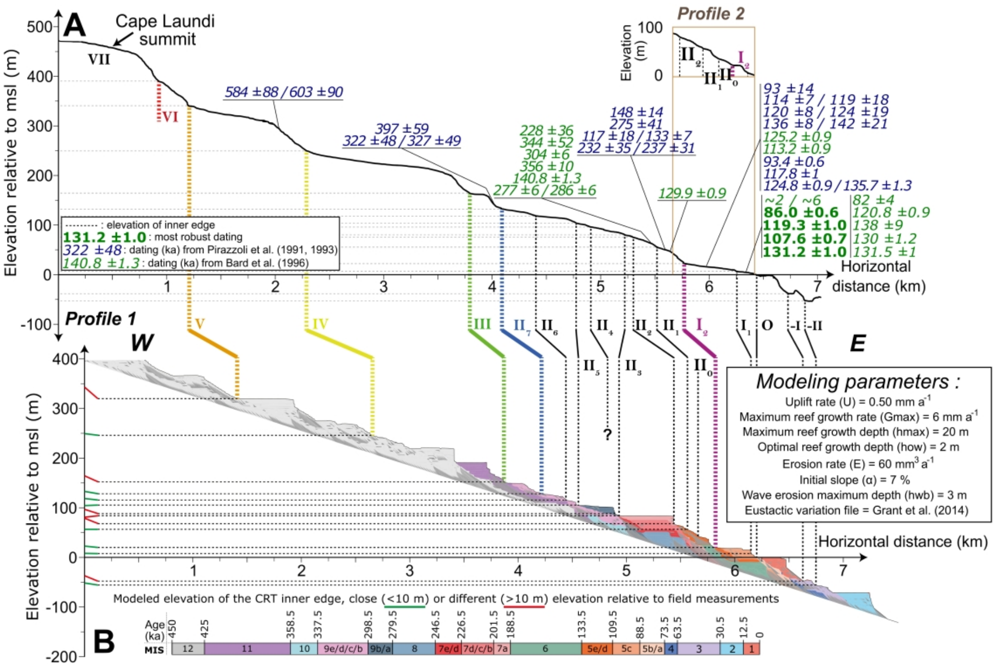

893x596mm (120 x 120 DPI)

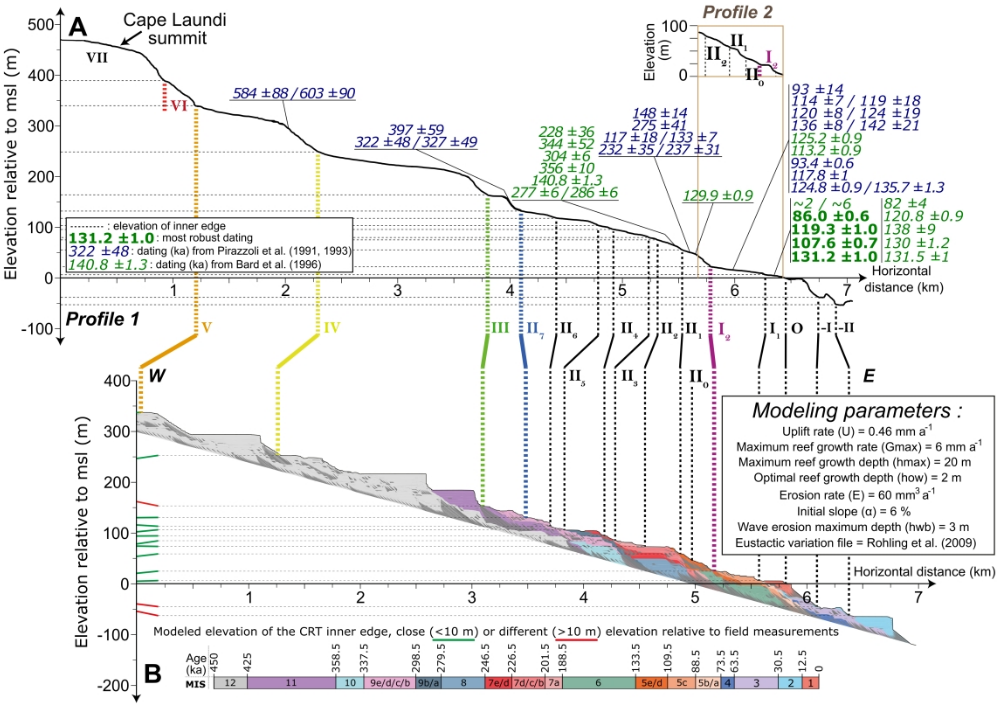

870x613mm (120 x 120 DPI)

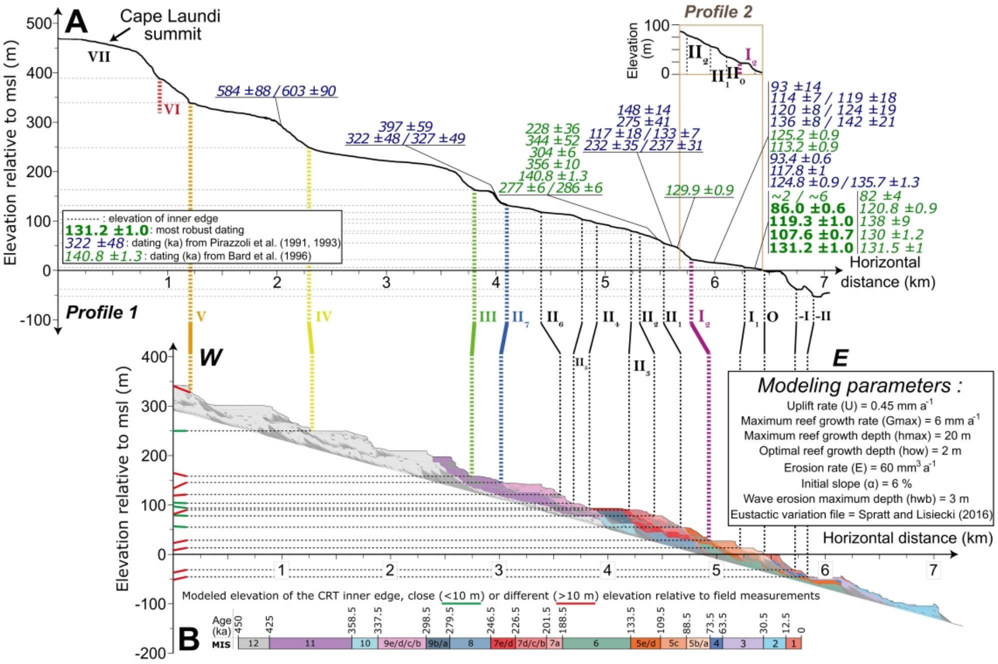

893x590mm (120 x 120 DPI)

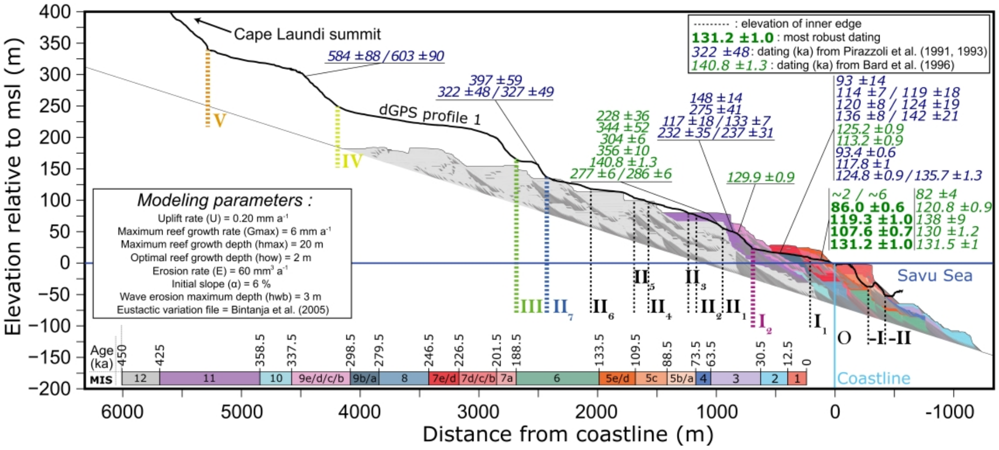

1100x493mm (120 x 120 DPI)

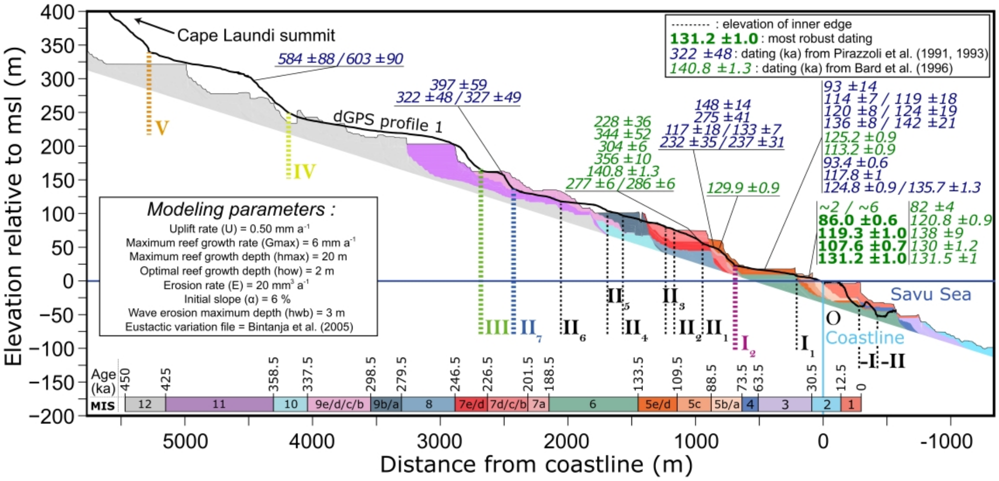

1389x672mm (120 x 120 DPI)

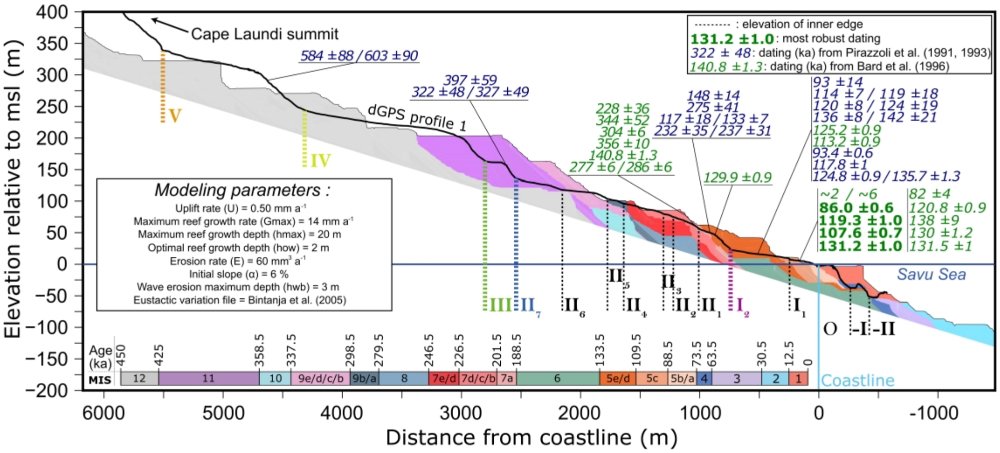

1426x642mm (120 x 120 DPI)

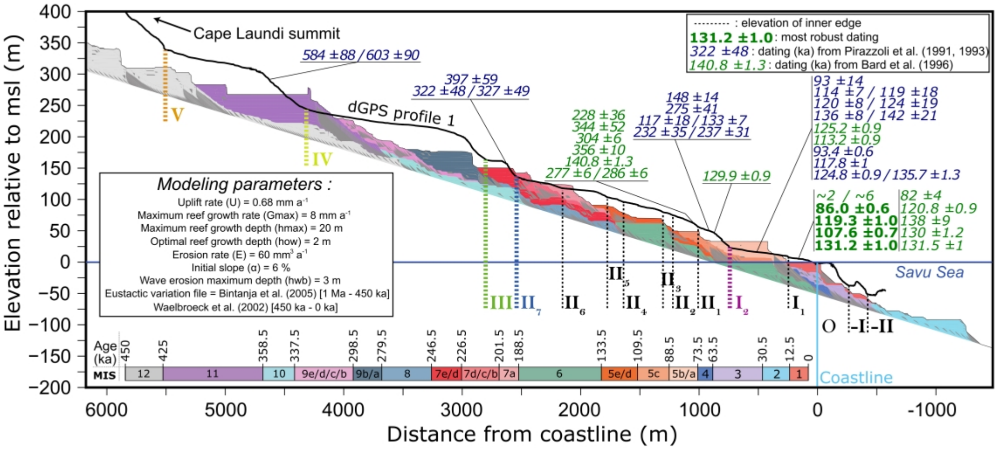

1101x494mm (120 x 120 DPI)